

P-functionalization of Ni Fe – Electrocatalysts from Prussian blue analogue for enhanced anode in anion exchange membrane water electrolyzers

Beatrice Ricciardi ^{a,b}, Williane da Silva Freitas ^a, Barbara Mecheri ^{a,*}, José Manuel Luque-Centeno ^{b,c}, Cinthia Alegre ^{b,*}, David Sebastián ^b, María Jesús Lázaro ^b, Alessandra D'Epifanio ^a

^a Department of Chemical Sciences and Technologies, University of Rome Tor Vergata, Via della Ricerca Scientifica, 00133 Rome, Italy

^b Instituto de Carboquímica, CSIC, Calle Miguel Luesma Castán 4, 50018 Zaragoza, Spain

^c Institute of Materials Science (ICMS, CSIC), Centro de Investigaciones Científicas Isla de La Cartuja. C/Américo Vespucio, 49, 41092 Sevilla, Spain

ARTICLE INFO

Keywords:

Platinum-group-metal-free electrocatalysts
Oxygen evolution reaction
Prussian blue analogues
NiFe-based catalyst
Phosphorus doping
Anion exchange membrane water electrolyzers

ABSTRACT

Efficient hydrogen generation from water-splitting is widely acknowledged as a priority route to promote the hydrogen economy. Anion exchange membrane water electrolyzers (AEMWE) offer multiple advantages in improving performance and minimizing the cost limitations of current electrolysis technologies. However, the persistence of issues related to the limited electrocatalytic activity of such materials and their poor stability under operating conditions makes developing highly active, stable, platinum-group-metal-free electrocatalysts for oxygen evolution reaction (OER) necessary.

We report the development of Prussian blue analogues (PBA)-derived NiFe-based electrocatalysts through a mild aqueous phase precipitation method, followed by thermal stabilization and phosphorus doping. The formation of the NiFe-PBA-precursor with a framework nanocubic $\text{Ni}(\text{II})[\text{Fe}(\text{III})(\text{CN})_6]_{2/3}$ structure was confirmed by X-ray diffraction, scanning electron microscopy, and inductively coupled plasma analysis. The NiFe-PBA-precursor was subjected to thermal stabilization and phosphorus doping to provide the material with enhanced OER catalytic activity and stability. The existence of OER active sites based on NiFe and NiFeP has been revealed by transmission electron microscopy, X-ray photoelectron spectroscopy, and electrochemical characterization in a three-electrode cell configuration in a 1 M KOH electrolyte. NiFe-PBA and NiFeP-PBA were assembled at the anode side of an AEMWE, resulting in an excellent electrochemical performance both in terms of current density at 2.0 V using 1 M KOH (1.21 A cm^{-2}) and durability, outperforming the benchmark catalyst.

1. Introduction

In the coming years, the decarbonization process must be urgently addressed in line with the growing energy demand.^[1] For these reasons, many efforts are increasingly focused on developing sustainable energy storage and conversion technologies, such as fuel cells and batteries, that can meet net-zero emission requirements with high performance.^[2–13] In this scenario, hydrogen production has become strategic in this global energy transition. Indeed, H₂ is an advantageous energy carrier ready to convert renewable but intermittent sources into energy-dense hydrogen fuels that can be stored and used in transportation and industrial processes.^[14–16]

Producing green hydrogen by water electrolysis technologies (WEs) at low temperature (<100 °C) is considered an efficient, clean, and long-

term solution.^[17] Among WEs, proton exchange membrane water electrolyzer (PEMWE) and the emerging anion exchange membrane water electrolyzer (AEMWE) are the promising ones.^[18] AEMWEs are particularly interesting because, in these devices, the advantages of more mature technologies are combined: key components without platinum-group-metal (PGM) materials like the alkaline WEs (AWEs) and high purity H₂ (99.99 %) production at a high current and high pressure like in PEMWEs. Another critical aspect of an AEMWE is that it can be fed with pure water or a low-alkalinity solution as the electrolyte. This results in reduced equipment corrosion and lower costs, thus improving the life of the electrolyzer.^[19–23]

One of the major bottlenecks in AEMWEs is the limiting oxygen evolution reaction (OER) catalysis, so overcoming it with a favorable kinetic catalyst is paramount. Ruthenium dioxide (RuO₂) and iridium

* Corresponding authors.

E-mail addresses: barbara.mecheri@uniroma2.it (B. Mecheri), cinthia@icb.csic.es (C. Alegre).

dioxide (IrO_2), belonging to PGM materials, are considered benchmark catalysts for OER due to their efficiency and low overpotentials (η). [24] However, large-scale applications are limited due to their stability problems (especially with acid electrolytes), high costs, and environmental impact.

Several PGM-free electrocatalysts have been proposed to improve OER electrocatalytic activity, lower the overpotential, and further improve the energy efficiency of AEMWEs. [25–29] Transition metal (TM)-based structures, such as oxides, carbides, nitrides, phosphides, phosphates, sulfides, and chalcogenides have been investigated to replace PGM materials. [19,30–36] Among the different families, TM-based oxides (TMOs), chalcogenides (TMCs), and phosphides (TMPs) are particularly promising since they offer the possibility of tailoring the electrocatalytic activity via heteroatom doping [37,38], the introduction of polymetallic sites [39–42], compounding with highly conductive materials [43], stress engineering [44] and heterostructure engineering. [45,46] Previous studies indicated that TMPs are particularly suited as OER electrocatalysts for water electrolysis due to their abundance and efficient electrocatalysis. [32,34,47–50] Metal phosphides doped with heteroatoms, rather than monometallic phosphides, have demonstrated improved catalytic activity due to the modified electronic structures, with the choice of TM playing a critical role. [51] Combining Ni with other TMs (e.g. Fe, Co, Mn, etc.) significantly improves OER activity in alkaline media [52–61], and, in particular, Fe-Ni-based catalysts have attracted attention due to their excellent results and low environmental impact. [56,57,62–65].

A crucial aspect in the development of an efficient electroactive catalyst is the design of its structure/morphology. Using metal-organic frameworks (MOFs) allows for precise tuning of crystal structure, with ligand type and metal geometry playing key roles in the overall catalytic performance of the final material. [66–68] As a subcategory of MOFs, prussian blue analogues (PBA) are coordination polymers assembled from octahedral coordination cyanide bridge metal nodes with a parent structure of $M[M'(\text{CN})_6]$ where M and M' are transition metals (TM). Among PBAs, hexacyanoferrates ($\text{Fe}(\text{CN})_6^{3-}$) offer a wide selection of metal nodes, microporous nature, and unique vacancy/defect arrangement. [69] The typical composition of hexacyanoferrates can be expressed as $M_x[\text{Fe}(\text{CN})_6]_y$, where M is commonly a transition metal (TM), such as Ni, Co, Fe, or Mn. [70] When the choice of metals and their oxidation state are varied, it is possible to alter the lattice parameters by stretching the hexacyanometallates structure to compensate for electroneutrality. [71,72] Nanostructured PBAs have recently been converted into metal oxides, sulfides, and functional phosphides while retaining their electron transfer properties. The synthesis, which generally takes place by chemical precipitation under soft conditions, allows extensive control over the composition of the material. [73–76] Moreover, the open skeleton structure composed of cyanide ligands and metal central ions enables the formation of uniformly distributed and adjustable metal active sites that can be tailored for specific electrochemical reactions. [77–79] Based on these features, PBAs have been recently evaluated for environmental and energy applications, such as sensors, contaminant removal, metal-ion batteries, and water splitting [80–87].

In this work, we developed PBA-derived NiFe-based electrocatalysts and investigated their performance as electrocatalysts for OER in AEMWEs. The synthesis occurs under mild conditions in an aqueous environment at room temperature, obtaining a PBA precursor with $\text{Ni}^{(\text{II})}[\text{Fe}^{(\text{III})}(\text{CN})_6]_{2/3}$ as crystal structure. To overcome the intrinsic limits of the PBA precursor in terms of limited electronic conductivity and electrochemical stability, it was thermally treated at 350 °C under inert conditions in the presence of a P-precursor for heteroatom doping. Through a series of morphological, structural, and electrochemical characterizations, the optimized electrocatalysts were assembled in AEMWE, demonstrating high OER activity and stability.

2. Material and methods

2.1. Materials

Nickel (II) acetate tetrahydrate (>99.9 %), trisodium citrate dihydrate (>99.0 %), potassium ferricyanide (III) (>99.9 %), sodium hypophosphite monohydrate (>99.9 %), IrO_2 (>99.9 %) and Nafion solution (5 wt% in lower aliphatic alcohols and water, 15–20 %), 2-propanol (99.9 %) were purchased from Sigma-Aldrich. Millipore water (18.2 MΩ cm@25 °C) was used for material preparation and experiments.

2.2. Synthesis of the electrocatalysts

1.92 g of nickel (II) acetate tetrahydrate $\text{Ni}(\text{CH}_3\text{COO})_2$ and 2.26 g of trisodium citrate dihydrate were solubilized in 50 mL of deionized under stirring at room temperature (about 250 rpm). Then, 50 mL of a 64 mM $\text{K}_3\text{Fe}(\text{CN})_6$ aqueous solution was added and kept stirring at room temperature overnight. The obtained precipitate was collected, centrifuged, washed, and dried at 70 °C and labeled as NiFe-PBA-precursor.

NiFe-PBA-precursor was heat-treated at 350 °C (3 °C min⁻¹ heating rate) for 2 h under N_2 flow, obtaining the sample labeled as NiFe-PBA. A further sample was obtained by using sodium hypophosphite (NaH_2PO_2) as a P-doping agent during the thermal treatment. As shown in Fig. S1, this process is carried out with two shuttles, one containing NaH_2PO_2 (upstream to the N_2 flow) and one containing NiFe-PBA-precursor (downstream), with a mass ratio of 2:1, respectively. The obtained sample was labeled as NiFeP-PBA.

2.3. Material characterization

Element quantification was performed by atomic emission spectroscopy on the Spectroblue TI FMT26 inductively coupled plasma – optical emission spectroscopy (ICP-OES) equipment. Before analysis, the sample was dried in an oven at 120 °C for two hours. Once dried, it was homogenized and grounded in an agate mortar. The mixture was then digested by oxidative alkaline fusion with sodium peroxide, followed by acid dilution with HCl to obtain a solution. Finally, this solution was filtered with a 0.45 μm pore size filter. Besides, Elemental Analysis (C, H, N) was determined on a Thermo Flash 1112 Elemental Analyser.

Transmission electron microscope (TEM) images and selected-area electron diffraction (SAED) pattern were acquired with a Tecnai F30 microscope operated at 300 kV, alongside images obtained in the scanning transmission mode with a high-angle annular dark-field detector (STEM-HAADF). The samples were ultrasonically dispersed in ethanol for 15 min and then placed in a Cu carbon grid. On the other hand, Scanning Electron Micrographs (SEM) were obtained using a Leo Supra 35 field-emission scanning electron microscope (Carl Zeiss, Oberkochen, Germany).

Powder X-ray diffraction (XRD) patterns were recorded using a Philips PW1730 and ESCAPlus of Omicron diffractometers with Cu K α radiation ($\lambda = 1.5406 \text{ \AA}$). Thermogravimetric analysis (TGA) was performed by using a thermogravimetric analyzer TGA/DSC1 Star System (Mettler Toledo) working between 25 to 700 °C under an N_2 flow, with a heating rate of 5 °C min⁻¹. The materials were held in a platinum sample holder with a cover having one central vent hole.

X-ray photoelectron spectra (XPS) were obtained in a ESCA Plus Omicron spectrometer equipped with a hemispherical electron analyzer with an Al anode (1486.7 eV) at 225 W with passing energy of 50 eV in the survey analysis and 20 eV in the high-resolution regions. The C 1 s line at 284.6 eV was employed for charge correction of all XPS spectra. CasaXPS software was used to perform peak fitting and quantification, and Shirley-type background was used for all peaks. A 70 %/30 % Gaussian/Lorentzian line shape was used to deconvolute the high resolution spectrum for each component.

Electrochemical tests were performed using a standard three-

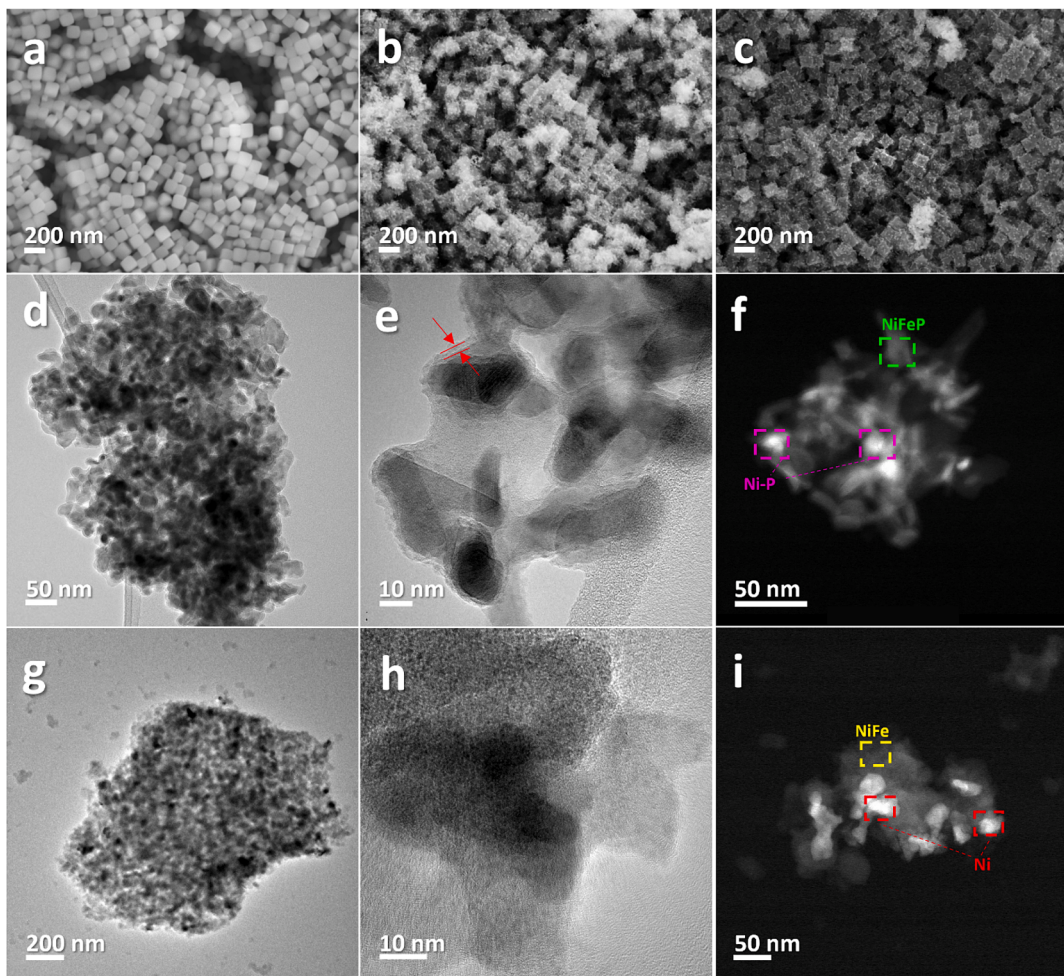


Fig. 1. SEM images of (a) NiFe-PBA-precursor, (b) NiFe-PBA, and (c) NiFeP-PBA. (d-e) TEM and (f) HAADF-STEM of NiFeP-PBA, (g-h) TEM and (i) HAADF-STEM of NiFe-PBA.

electrode cell: a rotating disk electrode setup (636 PAR AMETEK) with a rotating disc electrode (RDE-GC5009 Pine Research) or a rotating ring disc electrode (RRDE-AFE6R2GCPT, Pine Research) as the working electrodes (WE), while a graphite rod was used as the counter electrode (CE) and a Hg|HgO (RE – F0038) as the reference electrode (RE). Measurements were recorded with a VMP3 potentiostat (Bio-Logic Science Instruments) controlled by a computer using EC-Lab V10.18 software. Potential values for all electrochemical tests were measured against Hg|HgO and converted to the reversible hydrogen electrode (RHE), using the Nernst equation $E_{\text{RHE}} = E_{\text{Hg}|\text{HgO}} + 0.154 \text{ V} + 0.059 \times \text{pH}$, and the overpotential (η) value was determined by $\eta = E_{\text{RHE}} - 1.23 \text{ V}$.

Before the electrochemical tests, the WE was polished with an alumina slurry (0.3 μm particle size). The catalytic inks were prepared by dispersing 3.4 mg of catalyst in 425 ml of 2-propanol solution and 75 μl of Nafion/H₂O (0.5 wt%). The suspension was ultrasonicated for 15 min at room temperature. The ink was then drop-casted onto the WE glassy carbon disk at a catalyst loading of 0.20 mg cm⁻² and dried at room temperature. IrO₂ was used as a reference catalyst for OER. The IrO₂ ink was prepared using 1 mg of IrO₂ (99.9 %), 150 μl of 2-propanol, 14 μl of water and 6 μl of Nafion (5 wt%). The suspension was ultrasonicated for 15–20 min. The total IrO₂ loading was 0.2 mg cm⁻².

The tests were carried out in a three-electrode configuration with 1 M KOH as an electrolyte solution, purged with N₂ for 20 min. Before testing, the catalysts were activated by cyclic voltammetry (CV) in a potential window of 1.2 to 0.6 V vs. RHE at a scan rate of 50 mV s⁻¹ (25 cycles). To investigate the synthesized catalysts' electrochemical active

surface area (ECSA), cyclic voltammetry (CV) experiments were performed using an RDE in a static configuration. Gravimetric capacitance (C_{Grav}) was determined by integrating the capacitive current from the CV curves at a scan rate of 5 mV s⁻¹, in an N₂-saturated electrolyte over a potential window of 0.02 V to −0.1 V vs. RHE, according to the following equation [88]:

$$C_{\text{Grav}} = \frac{\int IdV}{2mv\Delta V} \quad (1)$$

Where i is the current (A), ΔV is the potential window (V), m is the mass of catalyst on the electrode (g) and v (V s⁻¹) is the potential scan rate. Thus, the ECSA was estimated based on Eq. (2), assuming a capacitance per surface area (Cs) of 0.04 mF cm⁻².[89]

$$\text{ECSA} = \frac{C_{\text{Grav}}}{C_s} \quad (2)$$

Linear sweep voltammetry (LSV) curves were acquired with RDE to evaluate the performance of the OER. Experiments were conducted at a scan rate of 10 mV s⁻¹ and a rotational speed of 1600 rpm from 1.7 to 1.0 V vs. RHE under N₂-saturated conditions to evaluate the OER. Disk currents were corrected from the background by subtracting the capacitive current measured in the N₂-saturated electrolyte, and reported potentials were compensated with it (85 %). The LSV of the electrocatalytic electrode was converted into a Tafel plot using the overpotential (η) vs. $\log j$ relation ($\eta = b \log |J| + a$); the Tafel slope (b) reflects the reaction mechanism of the catalysts. Additionally,

chronopotentiometry (at $J = 10 \text{ mA cm}^{-2}$) and LSV were used to analyze the durability and activity of the most active electrocatalyst after and before the stability test. Electrochemical impedance spectroscopy (EIS) spectra were recorded at a current density of 10 mA cm^{-2} (corresponding to E_{J10}) over a frequency range of 50 kHz to 100 Hz at a 10 mV amplitude (rms). According to previous works [48,90], the faradaic oxygen efficiency was determined by chronoamperometry measurement at 1 mA cm^{-2} , polarizing the Pt ring electrode at 0.4 V vs. RHE for promoting the oxygen reduction reaction (ORR). The faradaic oxygen efficiency ϵ was estimated using the following expression: $\epsilon = (4/n_{\text{O}_2}) \cdot i_{\text{disk}} / (N \cdot i_{\text{disk}})$, where n_{O_2} indicates the number of electrons transferred per O_2 molecule ($n_{\text{O}_2} = 4$ for the Pt ring), N is the RRDE collection efficiency (0.248).

2.4. MEA preparation and AEMWE tests

The tests in AEMWE were carried out using Pt/C as the cathode catalyst, while NiFeP-PBA, NiFe-PBA, and IrO₂ were used at the anode. The cathodes were made by spraying a catalytic ink based on Pt/C (40 wt% platinum on carbon, Alfa-Aesar) with 20 wt% FAA3 as ionomer (Fumion FAA-3-SOLUT-10, 10 wt% in *N*-methyl-2-pyrrolidone, FumaTech) onto a Sigracet 39 BC gas diffusion electrode to a Pt loading of 0.23 mg cm^{-2} .

The anodes were prepared by spraying the catalytic ink based on either IrO₂, NiFe-PBA, or NiFeP-PBA (20 % wt.% FAA3 ionomer) directly onto the anion exchange membrane (Fumasep® anionic membrane, FAA3-50, FumaTech) to obtain a catalyst-coated membrane (CCM). The catalyst loading was 1.6 for IrO₂ and 2 mg cm^{-2} for NiFe-PBA and NiFeP-PBA. The CCM was coupled with a Ni-fibre matrix (2Ni06-20, Bekaert) sheet to act as a porous transport layer at the anode side.

The cathode and CCM-membrane were combined into a Membrane-Electrode Assembly (MEA) by hot pressing (2.5 MPa, 60 °C, 5 min). Before testing, the MEA (bromide form) was exchanged using a 1 M KOH aqueous solution for 1 h, as previously reported. [91,92] Electrochemical characterizations were then carried out in a single-cell configuration (5 cm² geometric area of the electrodes) at 60 °C and atmospheric pressure. An aqueous electrolyte solution was supplied to the anode and the cathode sides (0.1–1 M KOH) with a flow rate of 6 mL min⁻¹. Electrochemical measurements for AEMWE were carried out using a PGSTAT302N potentiostat-galvanostat equipped with a 20 A booster (Metrohm). Polarization curves were obtained by varying the current from 0 to 1.6 A cm⁻² and measuring the cell voltage. Electrochemical impedance spectroscopy (EIS) analysis was used to determine the cell resistances. EIS was performed under potentiostatic conditions at a cell voltage of 1.5 V, in a frequency range of 1000 – 0.01 Hz, using frequency sweeps in single sinusoidal mode. Durability tests were carried out in 0.1 M KOH (changing it with a fresh electrolyte every 50 h) by setting a potential of 1.8 V and measuring the current over time.

3. Results and discussion

NiFe-PBA and NiFeP-PBA were obtained via a mild aqueous phase precipitation method, followed by thermal stabilization and phosphorus doping. First, a $M[\text{M}'(\text{CN})_6]$ precursor was obtained, using nickel(II) acetate as an M source and hexacyanoferrate(III) anion as $\text{M}'(\text{CN})_6$ source, in the presence of trisodium citrate for promoting the ion exchange process and precipitation of $\text{Ni}_3[\text{Fe}(\text{CN})_6]_2$ (NiFe-PBA-precursor). Thermal stabilization was carried out at 350 °C in an inert atmosphere without and with sodium hypophosphite, obtaining NiFe-PBA and the P-enriched analogous NiFeP-PBA.

Fig. 1 shows SEM and TEM images of NiFe-PBA-precursor, NiFe-PBA, and NiFeP-PBA, revealing the effect of heat treatment on the NiFe-PBA precursor at a morphological and compositional level. As can be seen in Fig. 1a, the NiFe-PBA-precursor is characterized by a cubic shape with edges of 150 nm; the cubic morphology is preserved even after the heat

treatment, as indicated by SEM images of NiFe-PBA and NiFeP-PBA (Fig. 1b and 1c, respectively). Based on the thermogravimetric analysis reported in Fig. S2, 350 °C as heat treatment temperature allows removing the thermally unstable phases while preserving the structure of the NiFe-PBA-precursor. In agreement with previous works investigating the effect of temperature on the catalytic activity of PBA-based compounds towards OER, the heat treatment is expected to promote the exposure of active sites, significantly improving the material's stability [93]. SEM images of NiFe-PBA and NiFeP-PBA revealed the presence of homogeneous cubic nanoparticles, which were studied in more detail by transmission electron microscopy (TEM).

Fig. 1d and 1g show TEM images of NiFeP-PBA and NiFe-PBA, respectively, indicating that the cubic nanoparticles are formed by agglomerates of smaller particles of homogeneous dimensions of approximately $\sim 30\text{--}40 \text{ nm}$, corresponding to the lighter areas in HAADF images (Fig. 1f and 1i) and consist of NiP- and Ni-based (violet and red dashed areas respectively) and NiFeP and NiFe-based nanoparticles (green and yellow dashed area). At higher magnifications (Fig. 1e and 1h), the nanoparticles in NiFeP-PBA appear to be more sharply defined than in NiFe-PBA. TEM-HAADF analysis also confirmed the effectiveness of P-functionalization in the NiFeP-PBA sample. In particular, as indicated by the red arrows in Fig. 1e, the NiFeP-PBA sample shows a thin outer layer formation, which can be traced back to P. This finding can be explained since phosphine gas is released upon the thermal decomposition of sodium hypophosphite, covering the NiFe-PBA structure as previously highlighted by previous works reporting similar P-functionalization methods. [48,94,95]

Elemental analysis carried out on the samples indicated that carbon content is less than 4 wt%. The Ni, Fe, and P content in the samples was evaluated through Inductively Coupled Plasma Optical Emission Spectroscopy (ICP-OES) analysis and reported in Table 1.

In both samples, the Ni/Fe molar ratio is 3:2, in agreement with $\text{Ni}(\text{II})[\text{Fe}(\text{III})(\text{CN})_6]_{2/3}$ crystal structure. The XRD patterns of NiFe-PBA-precursor, NiFe-PBA, and NiFeP-PBA are shown in Fig. 2. The diffractogram of the NiFe-PBA-precursor corresponds to the pattern of the $\text{Ni}_3[\text{Fe}(\text{CN})_6]_2 \cdot \text{H}_2\text{O}$ face-centered cubic crystal structure (JCPDS sheet

Table 1
Ni, Fe, and P content in NiFe-PBA and NiFeP-PBA samples.

Sample	Ni (wt.%)	Fe (wt.%)	P (wt. %)
NiFe-PBA	27.0 ± 0.2	17.3 ± 0.7	—
NiFeP-PBA	26.3 ± 0.1	16.6 ± 0.3	11.6 ± 0.1

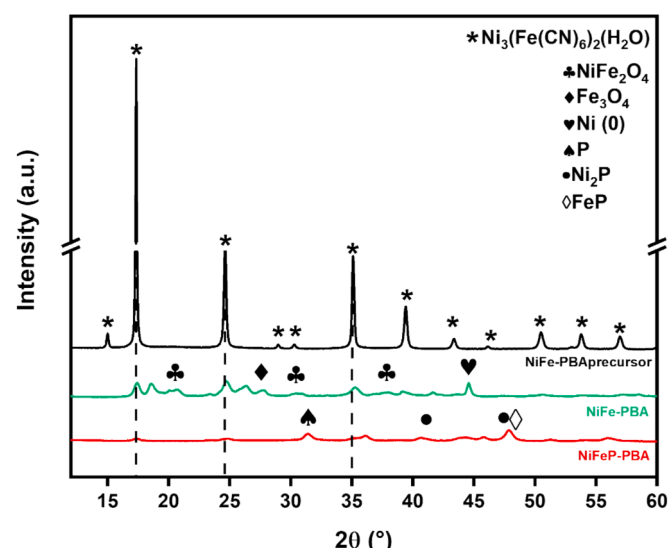


Fig. 2. X-ray diffractograms of NiFe-PBA-precursor, NiFe-PBA, and NiFeP-PBA.

No. 96–151-6493). As already predicted by TGA analysis (Fig. S2), after thermal treatment, NiFe-PBA and NiFeP-PBA partially retain the crystallinity of the precursor, as can be seen from the peaks at $2\theta = 17.4^\circ$, 24.6° , and 35.1° , but secondary metal phases were also observed. [87] The NiFe-PBA sample shows the presence of a nickel ferrite (NiFe_2O_4) phase (JCPDS sheet No. 96–901-0942) at $2\theta = 18.6^\circ$, 20.8° , and 39.3° and an iron (II, III) oxide (Fe_3O_4) phase (JCPDS sheet No. 96–901-4005) as can be seen from the peak at $2\theta = 27.9^\circ$. Additionally, the presence of Ni (0) (JCPDS 96–901-0942) at $2\theta = 44.6^\circ$ confirms the presence of metallic Ni, previously observed in HAADF-STEM analysis (Fig. 1i). The XRD pattern of NiFeP-PBA shows the presence of phosphorus (P) (JCPDS sheet No. 96–154–1405) at $2\theta = 31.4^\circ$. P-Ni and P-Fe phases are also observed as evidenced by Ni_2P nickel phosphide (JCPDS sheet no. 96–153–3385) at $2\theta = 40.7^\circ$, 47.8° (consistent with HAADF-STEM analysis Fig. 1f) and FeP (JCPDS sheet no. 96–152–8059) at $2\theta = 48.3^\circ$.

The surface stoichiometry of NiFe-PBA and NiFeP-PBA catalysts was determined by XPS (Fig. 3). Fig. 3a reveals the XPS survey spectra, indicating the presence of C, N, O, Fe, and Ni in NiFe-PBA and NiFeP-PBA, the latter including the presence of P. The deconvolution of Ni $2p_{3/2}$, Fe $2p_{3/2}$, and P $2p$ peaks are shown in Fig. 3b-d to investigate the element speciation. Table S1-3 shows the relative percentage of Ni, Fe, and P species and the associated binding energy (BE) obtained from the high-resolution XPS spectra of Ni $2p_{3/2}$, Fe $2p_{3/2}$, and P $2p$.

STEM images in Fig. S3a and S3c show the lattice fringes corresponding to NiP and P domains for the NiFeP-PBA sample, and Ni(0) and NiFe_2O_4 for the NiFe-PBA sample. The selected area electron diffraction (SAED) patterns are shown in Fig. S3b and S3d, corroborating the polycrystalline nature of both NiFe-PBA and NiFeP-PBA, as highlighted by HAADF-STEM images in Fig. 1, and XRD analysis (Fig. 2). Compared

to the bulk crystal structure observed by XRD, SAED patterns indicate that the arrangement of atoms on the near surface is slightly more amorphous, as envisaged from the wider broadening of the concentric circles. This effect is related to the heat treatment, particularly evident in NiFeP-PBA sample, where the reduced presence of lattice interference patterns suggests the homogeneous presence of an amorphous phosphorus layer.

Ni(II) was observed at 855.3 eV in the NiFe-PBA sample, which agrees with the presence of nickel ferrite (NiFe_2O_4) as revealed by XRD analysis. The Ni $2p_{3/2}$ deconvolution of NiFe-PBA also indicated the presence of Ni(0) at BE of 852.3 eV. This phase is associated with metal Ni and Ni-Fe alloy phases, in good agreement with XRD and HAADF-EDS analysis. The NiFeP-PBA sample shows the presence of Ni(II) (856.6 eV), with a minor contribution of Ni(III) (862.3 eV). The formation of Ni-P bonds, evident from HAADF-EDS and XRD analysis, was confirmed by the deconvoluted Ni 2p peaks at 852.9 eV.

For NiFeP-PBA and NiFe-PBA, iron is mainly distributed as Fe (III), with a lower percentage of Fe (II), confirming the partial preservation of the structure of the starting NiFe-PBA-precursor. NiFe-PBA also indicated the presence of Fe (0), which can be observed from the peak at 707.4 eV BE, while the occurrence of Fe-P bonds is evident for the NiFeP-PBA sample.

Deconvolution of the P $2p$ spectrum shows the presence of the peaks associated with P $2p_{3/2}$ and P $2p_{1/2}$ at 128.8 eV and 129.8 eV, as well as the presence of C-P / P-O (132.7 eV and 133.7 eV, respectively) and C-O-P (134.7 eV and 135.7 eV), compatible with phosphide, phosphorus oxide, and phosphorus bound to the partially preserved structure of the NiFe-PBA-precursor. [96–98]

Fig. 4 shows the electrochemical characterization of the NiFe-PBA

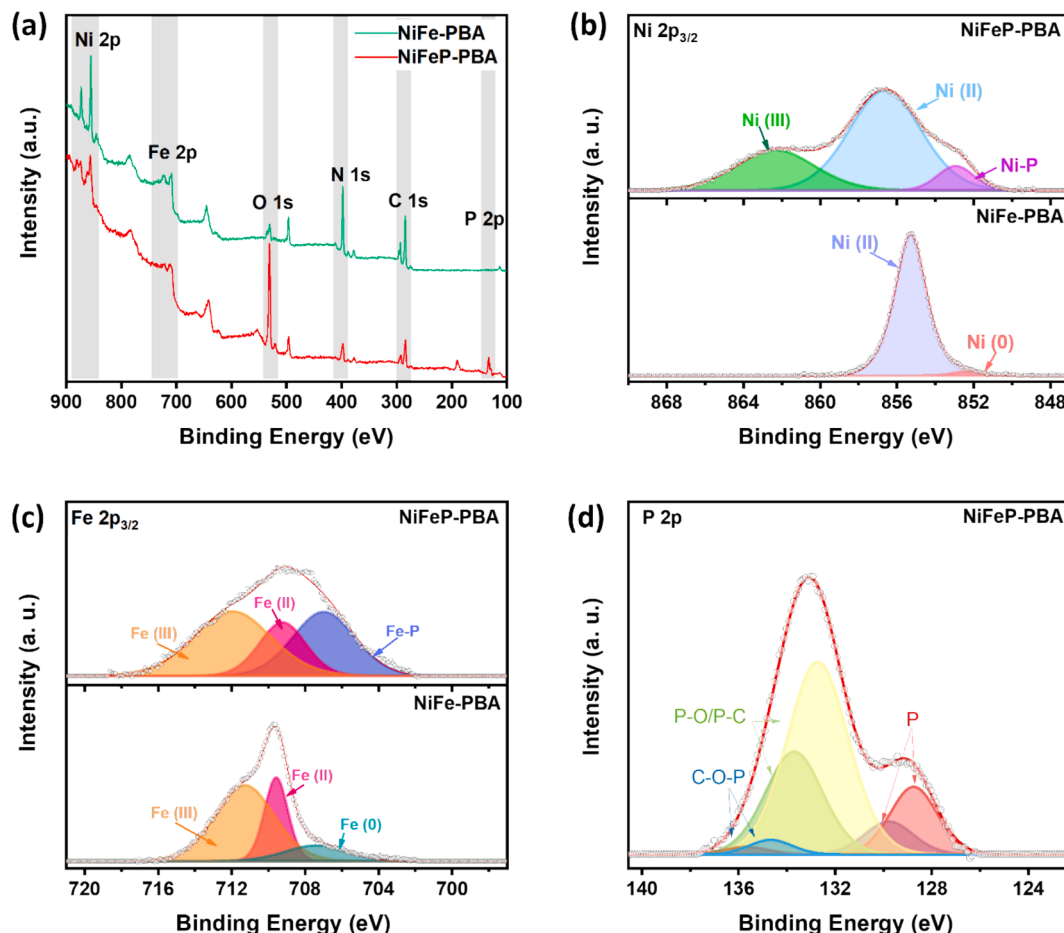


Fig. 3. XPS survey scans of NiFe-PBA and NiFeP-PBA (a), deconvoluted high-resolution XPS spectra for Ni $2p$ (b), Fe $2p$ (c), and P $2p$ (d).

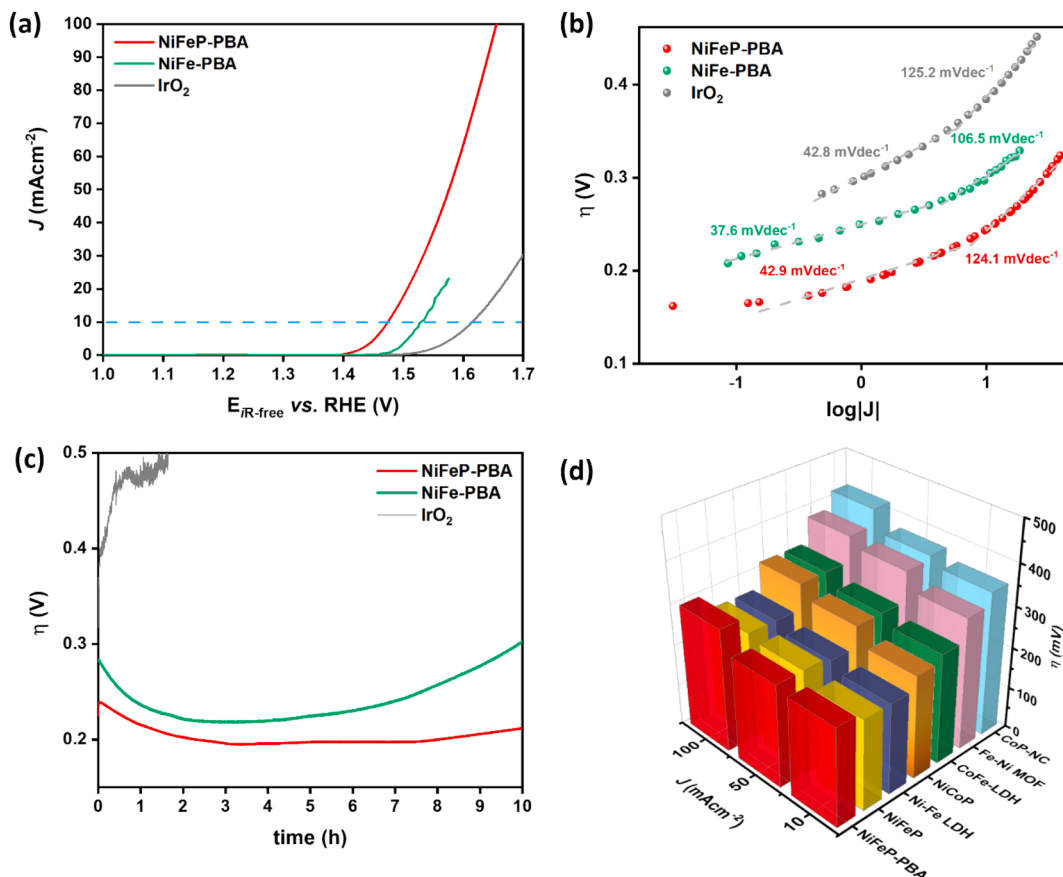


Fig. 4. (a) Polarization curves of IrO_2 , NiFe-PBA, and NiFeP-PBA at 10 mVs^{-1} , 1600 rpm in 1 M KOH; (b) Tafel slope of NiFeP-PBA, NiFe-PBA, and IrO_2 , (c) chronopotentiometry test at 10 mA cm^{-2} under dynamic conditions (1600 rpm), and (d) literature performance comparison ($\eta@10, 50, 100 \text{ mA cm}^{-2}$) for similar systems: NiFeP [104], Ni-Fe LDH [105], NiCoP [106], CoFe-LDH [107], Fe-Ni MOF [108], CoP-NC [94].

and NiFeP-PBA samples in a half-cell configuration using 1.0 M KOH as an electrolyte solution, and a performance comparison with literature data obtained for similar PGM-free catalysts. Hydrodynamic voltammetry with RDE was carried out to evaluate the OER activity of the NiFeP-PBA and NiFe-PBA samples, and Fig. 4a shows the polarization curves of NiFeP-PBA and NiFe-PBA compared with that of IrO_2 catalyst that represents, together with RuO_2 , the benchmark electrocatalysts for OER.[99] Potential values at 10 mA cm^{-2} current density of (E_{J10}) are 1.47 V and 1.52 V vs. RHE for NiFeP-PBA and NiFe-PBA, respectively. Both values outperformed the activity of the commercial IrO_2 , which instead has an $E_{J10} = 1.61 \text{ V}$ vs. RHE. The NiFeP-PBA showed a decreased overpotential for OER (50 mV) compared to NiFe-PBA, suggesting that P-functionalization boosts OER activity. As previously observed by Grimaud and coworkers, the anchoring of P sites on the active electrocatalytic interface promotes the oxidation of OH^- with the formation of the O-O bond by promoting interfacial transfer kinetics within the Helmholtz plane. [100,101].

The Tafel analysis (Fig. 4b) indicated two slopes for both catalysts: one around $\sim 40 \text{ mV dec}^{-1}$ (37.6 mV dec^{-1} for NiFe-PBA and 42.9 mV dec^{-1} for NiFeP-PBA) and another one around $\sim 118 \text{ mV dec}^{-1}$ ($106.5 \text{ mV dec}^{-1}$ for NiFe-PBA and $124.1 \text{ mV dec}^{-1}$ for NiFeP-PBA). The first slope can be associated with the dominant surface coverage of M at low overpotential, where M is the active site (Step A: $\text{M}^* \rightarrow \text{MOH}^*$), while the other is associated with oxygen deprotonation (Step B: $\text{MOH}^* \rightarrow \text{MO}$). This indicates a dependence on the surface coverage phase of M (step A), which requires high energy to form a new bond with oxygen. Step A, the rate-determining step is followed by favorable deprotonation (Step B). [102,103] Based on the similar values of Tafel slopes of NiFe-PBA and NiFeP-PBA, P-functionalization did not alter the OER mechanism, which

resulted in the same for NiFe-PBA and NiFeP-PBA.

The gravimetric capacitance of the two materials was calculated from the cyclic voltammograms shown in Fig. S4, according to Eq. (2), resulting 7.12 mF mg^{-1} and 5.12 mF mg^{-1} for NiFeP-PBA and NiFe-PBA, respectively. Considering a value of 0.04 mFc m^{-2} , ECSA resulted $17.8 \text{ m}^2 \text{ g}^{-1}$ and $13.0 \text{ m}^2 \text{ g}^{-1}$ for NiFeP-PBA and NiFe-PBA respectively. Those values are in agreement with other previously reported works dealing with similar materials.[109,110] The slightly higher ECSA of NiFeP-PBA than NiFe-PBA is coherent with the improved electrochemical activity of the P-functionalized sample. The Nyquist plots obtained by EIS and shown in Fig. S5 also confirm this trend. The first semicircle at higher frequencies is associated with electron transfer phenomena, as in the case of IrO_2 , the second semicircle is associated with mass transfer of OH^- , OOH^- functional species for the OER reaction.[111–113] P-functionalization allows for reducing both charge-transfer and mass-transfer resistances; this is also reflected in the higher faradic efficiency (ϵ) of NiFeP-PBA than NiFe-PBA. ϵ was evaluated by chronoamperometry (Fig. S6), being $\epsilon = 83\%$ for NiFeP-PBA and $\epsilon = 42\%$ NiFe-PBA.

Half-cell durability tests, shown in Fig. 4c, were performed by chronopotentiometry at 10 mA cm^{-2} under dynamic conditions (1600 rpm).[89] During the first two hours, η at 10 mA cm^{-2} (η_{J10}) decreases for both samples ($\sim 23\%$ for NiFe-PBA and $\sim 17\%$ for NiFeP-PBA) followed by an increase after 6 h for NiFe-PBA, while for NiFeP-PBA η_{J10} is maintained stable with only a slight increase after 10 h. The initial decrease can be attributed to the activation of the catalyst surface, which enhances the electrochemical kinetics as active sites become available. This phenomenon is often observed in the early stages of testing, where forming a thin layer of oxides or oxyhydroxides on the catalyst surface

increases catalytic activity. [114] As the test progresses, steady behavior indicates the active sites' stabilization, followed by only a slight increase after 6 h for NiFe-PBA and 10 h for NiFeP-PBA. By contrast, the rapid and immediate increase in overpotential in the case of IrO_2 indicates a significant material degradation in agreement with the literature. [79,80]

Fig. 4d shows a literature comparison of OER overpotential (η) at different current densities (10, 50, 100 mA cm^{-2}) with that of NiFeP-PBA reported in this work. In the literature landscape about OER electrocatalysts for AEMWEs, we can observe how the NiFeP-PBA catalyst is well-positioned regarding OER overpotential and electrocatalytic activity.

Based on the competitive electrochemical performance of NiFeP-PBA and NiFe-PBA, the catalysts were assembled at the anode of the AEMWE equipped with commercial Pt/C (40 wt. %) at the cathode of the single cell equipment, and a FAA3-50 Fumasep®. Schematics of AEMWE assembly is shown in Fig. 5a.

Fig. 5b shows the polarization curves for NiFeP-PBA, NiFe-PBA, and IrO_2 . The resulting trend is similar to those obtained in the half-cell tests. In fact, at 1.8 V, the NiFeP-PBA sample achieves a current density of 0.40 A cm^{-2} , while the current density for the MEAs equipped with NiFe-PBA and IrO_2 anode catalysts are 0.26 and 0.22 A cm^{-2} , respectively. In agreement with the Nyquist plots acquired in a half-cell configuration previously discussed in Fig. S5, the NiFeP-PBA exhibits polarization lower resistance ($0.63 \Omega \text{cm}^2$) than NiFe-PBA ($1.8 \Omega \text{cm}^2$), as highlighted by Nyquist plots obtained by EIS analysis under AEMWE operation (Fig. S7).

Fig. 5c shows the polarization curves of the NiFeP-PBA using different KOH concentrations (0.1 to 1 M). When KOH concentration is decreased, there is only a moderate decrease in electrochemical performance: the current density at 1.8 V decreased only about 40 % when the electrolyte concentration decreased by one order of magnitude.

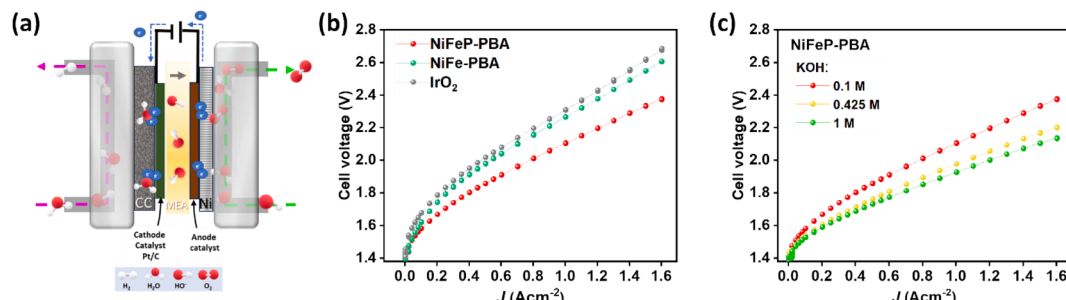


Fig. 5. (a) Schematics of an AEMWE assembly, (b) Polarization curves of NiFeP-PBA, NiFe-PBA, and IrO_2 samples (0.1 M KOH), (c) polarization curves of NiFeP-PBA at different KOH concentrations (0.1–1.0 M).

Table 2

Comparison of current density values obtained in this work and in the literature for AEMWEs equipped with PGM-free OER catalysts at the anodes.

AEM	Anode/Cathode (loading) catalysts	[KOH] (M)	J (A cm^{-2}) @1.8 V	J (A cm^{-2}) @2 V	T (°C)	Ref.
FAA-3-50	IrO_2 (1.6 mg cm^{-2}) / Pt/C(40 %) (0.23 mg cm^{-2})	0.1	0.22	0.79	60	This work
FAA-3-50	NiFe-PBA (2 mg cm^{-2}) / Pt/C(40 %) (0.23 mg cm^{-2})	0.1	0.26	0.54	60	This work
FAA-3-50	NiFe-PBA (1.9 mg cm^{-2}) / Pt/C(40 %) (0.23 mg cm^{-2})	0.1	0.40	0.47	60	This work
FAA-3-50	NiFe-PBA (1.9 mg cm^{-2}) / Pt/C(40 %) (0.23 mg cm^{-2})	0.425	0.59	1.06	60	This work
FAA-3-50	NiFe-PBA (1.9 mg cm^{-2}) / Pt/C(40 %) (0.23 mg cm^{-2})	1	0.67	1.21	60	This work
FAA-3-50	NiFe_2O_4 (1.8 mg cm^{-2}) / Raney nickel (14.8 mg cm^{-2})	1	0.24		60	[115]
SustainionGrade T	NiFe_2O_4 (1.8 mg cm^{-2}) / Raney nickel (14.8 mg cm^{-2})	1	0.84		60	[115]
FAA-3-50	NiFeOOH (0.5 mg cm^{-2}) / Pt/C (0.4 mg cm^{-2})	1		3.6 @1.9 V	70	[116]
FAA3-50	NiFeOx (3 mg cm^{-2}) / Pt/C (0.5 mg cm^{-2})	1	1.5	2.4	60	[117]
FAA3-50	NiFe_2O_4 (2 mg cm^{-2}) / NiFeCo (2 mg cm^{-2})	1	0.38		60	[118]
FAS-50	NiFe_2O_4 (1.8 mg cm^{-2}) / NiFeCo (2.7 mg cm^{-2})	1	0.24		60	[118]
FAA3-50	g-CN-CNF-800 (6 mg cm^{-2}) / Pt/C(40 %) (0.4 mg cm^{-2})	1		0.73 @1.9 V	60	[119]
FAA3-50	NiMn_2O_4 (3 mg cm^{-2}) / (0.5 mg cm^{-2})	1		0.530	80	[120]
FAA3-50	NiMn_2O_4 / CNF (2.5 mg cm^{-2}) / Pt/C(40 %) (0.5 mg cm^{-2})	6	0.18		60	[121]
FAA3-50	NiCo_2O_4 /CNF(3 mg cm^{-2}) / Pt/C(40 %) (0.5 mg cm^{-2})	6	0.30		60	[121]
Sustainion	NiFe_2O_4 / NiFeCo	1		1.6	60	[122]

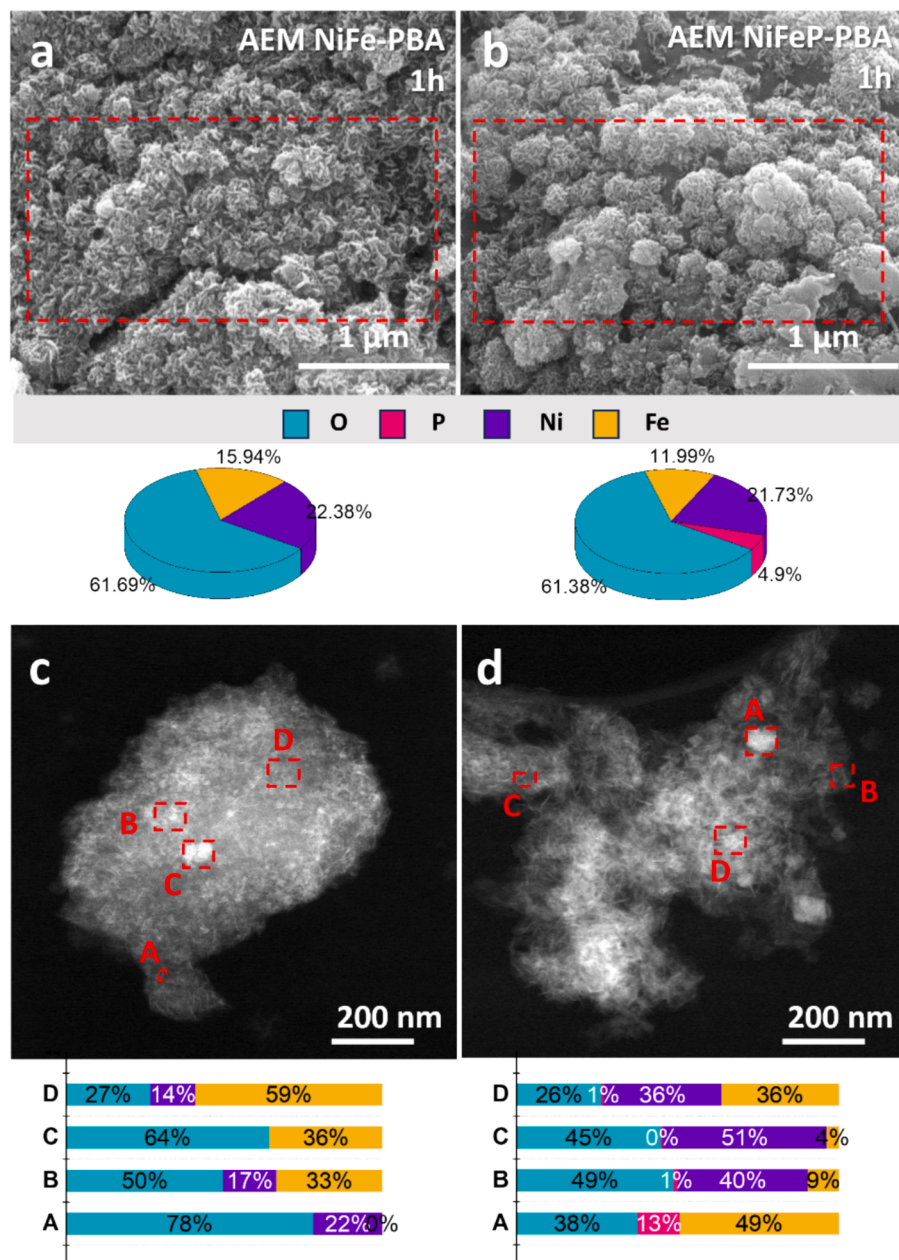


Fig. 6. SEM images of (a) NiFe-PBA, (b) NiFeP-PBA, and HAADF-STEM images of (c) NiFe-PBA, and (d) NiFeP-PBA after 1 h AEMWE operation with the corresponding element atomic percentage.

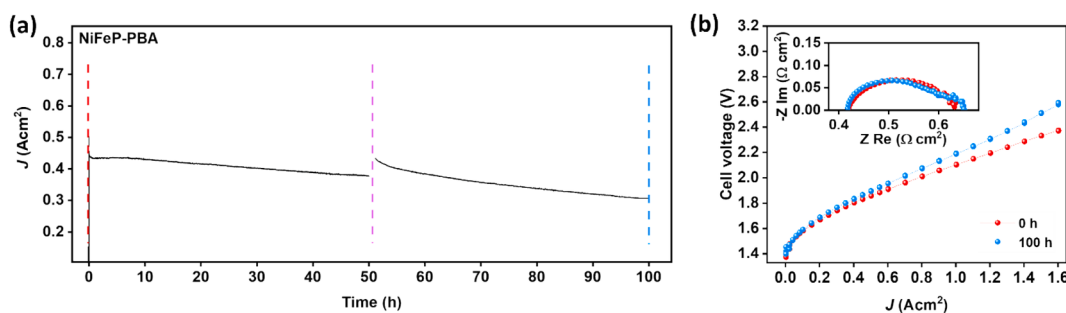


Fig. 7. (a) Durability test: $J@1.8$ V over time for NiFeP-PBA, and (b) the corresponding polarization curves and EIS spectra at 1.5 V (inset) before (0 h) and after (100 h) the durability test.

The current density loss is about 12 % after 50 h and 28 % after 100 h. The loss of performance over time has also been observed in similar systems, and this is not explicitly related to the anode catalyst itself but to the system as a whole. [127] Some major critical factors are related to the membrane used (in this case FAA-3–50 Fumasep®), [118] the ionomer binding agent, [128,129] pH, [130,131] electrolyte transport issues, [132] and other factors specific to the setup itself. [125] In fact, replacing the electrolyte with a fresh electrolyte after 50 h operation, which is a standard practice in AEMWE testing [125,133], positively influenced the test performance, which significantly improved (about 10 %) after the electrolyte change. This aspect indicates a partial reversible degradation associated with the system, particularly the electrolyte composition.

Polarization curves and EIS spectra were acquired before and after the durability test (Fig. 7b), resulting in only an 8 % increase in total polarization resistance, which allows for retaining up to 88 % current density at 1.8 V after 100 h of AEMWE working, which can be considered as a promising and competitive result as compared to previous published papers. [134,135] Therefore, NiFeP-PBA has demonstrated a high OER activity in an alkaline environment, resulting in a good performance in delivered current density and stability once assembled at the anode of an AEMWE.

4. Conclusion

Mild aqueous precipitation of iron and nickel PBA analogues followed by thermal stabilization in an inert gas atmosphere is a facile and efficient strategy for preparing NiFe-PBA OER catalysts in AEMWE applications. As highlighted by SEM, TEM, XRD, and XPS analysis, the thermal stabilization step enabled obtaining NiFe-based OER active sites distributed as Fe_3O_4 , NiFe_2O_4 , and metal nickel, preserving the nano cubic morphology of the $\text{Ni}[\text{Fe}(\text{CN})_6]_{2/3}$ precursor structure. Implementing the thermal treatment step with sodium hypophosphite allowed P-functionalization and the formation of NiFeP-based active sites to boost OER activity further. The electrochemical performances, evaluated by LSV-RDE and chronopotentiometry experiments in a half-cell configuration in 1 M KOH electrolyte, indicated E_{J10} of 1.47 V for NiFeP-PBA and 1.52 V vs. RHE for NiFe-PBA, with good performance stability over time. These values surpassed the IrO_2 performance used as a benchmark ($E_{J10} = 1.61$ V vs. RHE, huge stability loss).

Polarization curves obtained in the AEMWE (fuel-cell configuration) reflected the same trend observed in the half-cell, and the NiFeP-PBA sample delivered a current density of 1.21 A cm^{-2} at 2 V (1 M KOH). The electrochemical results were complemented by SEM and HAADF-STEM of the NiFe-PBA-based samples after AEMWE operation, suggesting a crucial role of PBA as catalyst precursor, thermal stabilization, and P-doping in enhancing the electrocatalyst activity and stability of the catalysts. The NiFeP-PBA, in addition to having better-performing polarization curves than NiFe-PBA, showed promising results in terms of stability by maintaining 88 % of the current density at 1.8 V after 100 h of operation in the AEMWE.

CRediT authorship contribution statement

Beatrice Ricciardi: Writing – review & editing, Writing – original draft, Methodology, Investigation, Data curation. **Williane da Silva Freitas:** Writing – review & editing, Validation, Methodology, Investigation, Data curation. **Barbara Mecheri:** Writing – review & editing, Visualization, Supervision, Resources, Project administration, Methodology, Investigation, Formal analysis, Conceptualization. **José Manuel Luque-Centeno:** Writing – review & editing, Supervision, Methodology, Data curation. **Cinthia Alegre:** Writing – review & editing, Visualization, Supervision, Resources, Project administration, Funding acquisition, Formal analysis, Data curation. **David Sebastián:** Writing – review & editing, Visualization, Resources, Methodology, Funding acquisition, Formal analysis, Data curation. **María Jesús Lázaro:** Project

administration, Funding acquisition. **Alessandra D'Epifanio:** Writing – review & editing, Resources, Methodology, Investigation, Funding acquisition, Conceptualization.

Declaration of competing interest

The authors declare that they have no known competing financial interests or personal relationships that could have appeared to influence the work reported in this paper.

Data availability

Data will be made available on request.

Acknowledgments

This work was partly supported by the Italian Ministry of Foreign Affairs and International Cooperation", grant number CN23GR06. This research was supported by MICIU/AEI/10.13039/501100011033 with funding from NextGenerationEU (PRTR-C17.II) within the Planes Complementarios con CCAA (Area of Green Hydrogen and Energy) and it has been carried out in the CSIC Interdisciplinary Thematic Platform (PTI +) Transición Energética Sostenible+ (PTI TRANSENER +), alongside funding to project (Ref. TED2021-130279A-I00) with funding also from the Next Generation EU Programme.

Appendix A. Supplementary data

Supplementary data to this article can be found online at <https://doi.org/10.1016/j.cej.2024.156256>.

References

- [1] J. Rissman, C. Bataille, E. Masanet, N. Aden, W.R. Morrow, N. Zhou, N. Elliott, R. Dell, N. Heeren, B. Huckestein, J. Cresko, S.A. Miller, J. Roy, P. Fennell, B. Creminns, T. Koch Blank, D. Hone, E.D. Williams, S. de la Rue du Can, B. Sisson, M. Williams, J. Katzenberger, D. Burtraw, G. Sethi, H. Ping, D. Danielson, H. Lu, T. Lorber, J. Dinkel, J. Helseth, Technologies and policies to decarbonize global industry: Review and assessment of mitigation drivers through 2070, *Appl. Energy* 266 (2020) 114848. doi: 10.1016/j.apenergy.2020.114848.
- [2] B. Ricciardi, B. Mecheri, W. da Silva Freitas, V.C.A. Ficca, E. Placidi, I. Gatto, A. Carbone, A. Capasso, A. D'Epifanio, Porous iron-nitrogen-carbon electrocatalysts for anion exchange membrane fuel cells (AEMFC), *ChemElectroChem* (2023) 1–12, <https://doi.org/10.1002/celec.20220115>.
- [3] M.M. Hossen, M.S. Hasan, M.R.I. Sardar, J. bin Haider, Mottakin, K. Tammeveski, P. Atanassov, State-of-the-art and developmental trends in platinum group metal-free cathode catalyst for anion exchange membrane fuel cell (AEMFC), *Appl. Catal. B Environ.* 325 (2022) 121733, <https://doi.org/10.1016/j.apcatb.2022.121733>.
- [4] S. He, B. Chen, C. Meng, F. Shi, A. Yuan, W. Miao, H. Zhou, Coupling NiSe₂ nanoparticles with N-doped porous carbon enables efficient and durable electrocatalytic hydrogen evolution reaction at pH values ranging from 0 to 14, *ACS Appl. Nano Mater.* 7 (2024) 1138–1145, <https://doi.org/10.1021/acsnano.3c05126>.
- [5] Y. Shen, S. He, Y. Zhuang, S. Huang, C. Meng, A. Yuan, W. Miao, H. Zhou, Polypyrrole template-assisted synthesis of tubular Fe-NC nanostructure-based electrocatalysts for efficient oxygen reduction reaction in rechargeable zinc-air battery, *ACS Appl. Nano Mater.* 6 (2023) 16873–16881, <https://doi.org/10.1021/acsnano.3c03056>.
- [6] B. Ricciardi, W. da Silva Freitas, B. Mecheri, K.U. Nisa, J. Montero, V.C.A. Ficca, E. Placidi, C. Alegre, A. D'Epifanio, Hierarchical porous Fe/Ni-based bifunctional oxygen electrocatalysts for rechargeable zinc-air batteries, *Carbon* n. y. 219 (2024), <https://doi.org/10.1016/j.carbon.2023.118781>, 118781.
- [7] J. Fagerström, S. Das, Ø.S. Klyve, V. Olkkonen, E.S. Marstein, Profitability of battery storage in hybrid hydropower–solar photovoltaic plants, *J. Energy Storage* 77 (2024), <https://doi.org/10.1016/j.est.2023.109827>, 109827.
- [8] V.C.A. Ficca, C. Santoro, E. Placidi, F. Arciprete, A. Serov, P. Atanassov, B. Mecheri, Exchange current density as an effective descriptor of poisoning of active sites in platinum group metal-free electrocatalysts for oxygen reduction reaction, *ACS Catal.* 13 (2023) 2162–2175, <https://doi.org/10.1021/acscatal.2c05222>.
- [9] W. da Silva Freitas, B. Mecheri, C. Lo Vecchio, I. Gatto, V. Baglio, V.C.A. Ficca, A. Patra, E. Placidi, A. D'Epifanio, Metal-organic-framework-derived electrocatalysts for alkaline polymer electrolyte fuel cells, *J. Power Sources* 550 (2022), <https://doi.org/10.1016/j.jpowsour.2022.232135>, 232135.

- [10] W. da Silva Freitas, D. Gemma, B. Mecheri, A. D'Epifanio, Air-breathing cathodes for microbial fuel cells based on iron-nitrogen-carbon electrocatalysts, *Bioelectrochemistry* 146 (2022), <https://doi.org/10.1016/j.bioelechem.2022.108103>, 108103.
- [11] J. Montero, W. da Silva Freitas, B. Mecheri, M. Forchetta, P. Galloni, S. Licoccia, A. D'Epifanio, A neutral-pH aqueous redox flow battery based on sustainable organic electrolytes, *ChemElectroChem* 10 (2023) 1–7, <https://doi.org/10.1002/celec.202201002>.
- [12] S. Zago, L.C. Scarpetta-Pizo, J.H. Zagal, S. Specchia, PGM-free biomass-derived electrocatalysts for oxygen reduction in energy conversion devices: promising materials, *Springer Nature Singapore* (2024), <https://doi.org/10.1007/s41918-023-00197-3>.
- [13] A. Cosenza, L. Delafontaine, A. Ly, H. Wang, E. Murphy, Y. Liu, S. Specchia, P. Atanassov, Novel acid-free process intensification for the synthesis of non-precious metal-nitrogen-carbon electrocatalysts for oxygen reduction reaction, *J. Power Sources* 556 (2023) 1–32, <https://doi.org/10.1016/j.jpowsour.2022.232382>.
- [14] Z. Abdin, Empowering the hydrogen economy: the transformative potential of blockchain technology, *Renew. Sustain. Energy Rev.* 200 (2024) 114572, <https://doi.org/10.1016/j.rser.2024.114572>.
- [15] X. Han, P. Vercoulen, S. Lee, A. Lam, S. Kato, T. Morotomi, Policy design for diffusing hydrogen economy and its impact on the Japanese economy for carbon neutrality by 2050: analysis using the E3ME-FTT model, *Energies* 16 (2023) 7392, <https://doi.org/10.3390/en16217392>.
- [16] B. Amini Horri, H. Ozcan, Green hydrogen production by water electrolysis: current status and challenges, *Curr. Opin. Green Sustain. Chem.* 47 (2024) 100932, <https://doi.org/10.1016/j.cogsc.2024.100932>.
- [17] M.A. Qadeer, X. Zhang, M.A. Farid, M. Tanveer, Y. Yan, S. Du, Z.F. Huang, M. Tahir, J.Z. Jou, A review on fundamentals for designing hydrogen evolution electrocatalyst, *J. Power Sources* 613 (2024) 234856, <https://doi.org/10.1016/j.jpowsour.2024.234856>.
- [18] C. Liu, Z. Geng, X. Wang, W. Liu, Y. Wang, Q. Xia, W. Li, L. Jin, C. Zhang, Development of advanced anion exchange membrane from the view of the performance of water electrolysis cell, *J. Energy Chem.* 90 (2024) 348–369, <https://doi.org/10.1016/j.jecchem.2023.11.026>.
- [19] M. Yu, E. Budiyanto, H. Tüysüz, Principles of water electrolysis and recent progress in Cobalt-, Nickel-, and iron-based oxides for the oxygen evolution reaction, *Angew. Chemie - Int. Ed.* 61 (2022) e202103824.
- [20] N. Du, C. Roy, R. Peach, M. Turnbull, S. Thiele, C. Bock, Anion-exchange membrane water electrolyzers, *Chem. Rev.* 122 (2022) 11830–11895, <https://doi.org/10.1021/acs.chemrev.1c00854>.
- [21] D. Hua, J. Huang, E. Fabbri, M. Rafique, B. Song, Development of anion exchange membrane water electrolysis and the associated challenges: a review, *ChemElectroChem* 10 (2023) e202200999.
- [22] Y. Sei Park, Y. Park, M. Je Jang, J. Lee, C. Kim, M. Gyu Park, J. Yang, J. Choi, H. Mo Lee, S. Mook Choi, Effect of intrinsic and extrinsic activity of electrocatalysts on anion exchange membrane water electrolyzer, *Chem. Eng. J.* 472 (2023) 145150, <https://doi.org/10.1016/j.cej.2023.145150>.
- [23] C. Santoro, A. Lavacchi, P. Mustarelli, V. Di Noto, L. Elbaz, D.R. Dekel, F. Jaouen, What is Next in anion-exchange membrane water electrolyzers? Bottlenecks, benefits, and future, *ChemSusChem* 15 (2022) e202200027.
- [24] C. Wei, R.R. Rao, J. Peng, B. Huang, I.E.L. Stephens, M. Risch, Z.J. Xu, Y. Shao-Horn, Recommended practices and benchmark activity for hydrogen and oxygen electrocatalysis in water splitting and fuel cells, *Adv. Mater.* 31 (2019) 1–24, <https://doi.org/10.1002/adma.201806296>.
- [25] N. Yu, J.Y. Lv, Z.C. Guo, X.J. Tian, Y.S. Zhang, W.J. Li, Y.L. Zhou, Y.M. Chai, B. Dong, Strong Lewis acid-induced self-healing of loose FeOOH for alkaline oxygen evolution, *Chem. Eng. J.* 487 (2024) 150253, <https://doi.org/10.1016/j.cej.2024.150253>.
- [26] L. Osmieri, H. Yu, R.P. Hermann, M.E. Kreider, H.M. Meyer, A.J. Kropf, J.H. Park, S.M. Alia, D.A. Cullen, D.J. Myers, P. Zelenay, Aerogel-derived nickel-iron oxide catalysts for oxygen evolution reaction in alkaline media, *Appl. Catal. B Environ.* 348 (2024) 123843, <https://doi.org/10.1016/j.apcatb.2024.123843>.
- [27] H. Yin, L. Qian, H. Xiao, L. Zhang, X. Li, X. Zhou, S. Yuan, C. Li, Q. Lu, F. Pan, L. Zeng, J. Guo, S. Li, Shock-endurable and reversible evolution between CoOOH and intermediate governed by interfacial strain for fluctuating oxygen evolution, *Chem. Eng. J.* 490 (2024) 151699, <https://doi.org/10.1016/j.cej.2024.151699>.
- [28] S. Han, J. Park, J. Yoon, Surface reconstruction of Co-based catalysts for enhanced oxygen evolution activity in anion exchange membrane water electrolysis, *Adv. Funct. Mater.* 2314573 (2024) 1–10, <https://doi.org/10.1002/adfm.202314573>.
- [29] K.Y. Yoon, K.B. Lee, J. Jeong, M.J. Kwak, D. Kim, H.Y. Roh, J.H. Lee, S.M. Choi, H. Lee, J. Yang, Improved oxygen evolution reaction kinetics with titanium incorporated nickel ferrite for efficient anion exchange membrane electrolysis, *ACS Catal.* 14 (2024) 4453–4462, <https://doi.org/10.1021/acs.catal.3c05761>.
- [30] X. Hu, S. Zhang, J. Sun, L. Yu, X. Qian, R. Hu, Y. Wang, H. Zhao, J. Zhu, 2D Fe-containing cobalt phosphide/cobalt oxide lateral heterostructure with enhanced activity for oxygen evolution reaction, *Nano Energy* 56 (2019) 109–117, <https://doi.org/10.1016/j.nanoen.2018.11.047>.
- [31] H. Yang, M. Driess, P.W. Menezes, Self-supported electrocatalysts for practical water electrolysis, *Adv. Energy Mater.* 11 (2021) 2102074, <https://doi.org/10.1002/aenm.202102074>.
- [32] L. Yang, R. Liu, L. Jiao, Electronic redistribution: construction and modulation of interface engineering on CoP for enhancing overall water splitting, *Adv. Funct. Mater.* 30 (2020) 1–8, <https://doi.org/10.1002/adfm.201909618>.
- [33] A. Parra-Puerto, K.L. Ng, K. Fahy, A.E. Goode, M.P. Ryan, A. Kucernak, Supported transition metal phosphides: activity survey for HER, ORR, OER, and corrosion resistance in acid and alkaline electrolytes, *ACS Catal.* 9 (2019) 11515–11529, <https://doi.org/10.1021/acscatal.9b03359>.
- [34] T. Zhang, K. Yang, C. Wang, S. Li, Q. Zhang, X. Chang, J. Li, S. Li, S. Jia, J. Wang, L. Fu, Nanometric Ni5P4 clusters nested on Ni₂O₃ for efficient hydrogen production via alkaline water electrolysis, *Adv. Energy Mater.* 8 (2018) 4–9, <https://doi.org/10.1002/aenm.201801690>.
- [35] S. Ananthraj, J. Kennedy, S. Kundu, Microwave-Initiated facile formation of Ni₃Se₄ nanoassemblies for enhanced and stable water splitting in neutral and alkaline media, *ACS Appl. Mater. Interfaces* 9 (2017) 8714–8728, <https://doi.org/10.1021/acsami.6b15980>.
- [36] Y.S. Park, J. Jeong, Y. Noh, M.J. Jang, J. Lee, K.H. Lee, D.C. Lim, M.H. Seo, W. B. Kim, J. Yang, S.M. Choi, Commercial anion exchange membrane water electrolyzer stack through non-precious metal electrocatalysts, *Appl. Catal. B Environ.* 292 (2021) 120170, <https://doi.org/10.1016/j.apcatb.2021.120170>.
- [37] I.S. Amiuin, Z. Pu, X. Liu, K.A. Owusu, H.G.R. Monestel, F.O. Boakye, H. Zhang, S. Mu, Multifunctional Mo-N/C@MoS₂ electrocatalysts for HER, OER, ORR, and Zn–Air batteries, *Adv. Funct. Mater.* 27 (2017) 1–11, <https://doi.org/10.1002/adfm.201702300>.
- [38] W. Yoshimura, J.B. Falqueto, A.H. Clark, N.S. Yüzbaşı, T. Graule, D. Baster, M. El Kazzi, T.J. Schmidt, E. Fabbri, The role of phosphate functionalization on the oxygen evolution reaction activity of cobalt-based oxides at different pH values, *Small Struct.* 4 (2023) 1–10, <https://doi.org/10.1002/sstr.202300106>.
- [39] E. Charnetskaya, T.D. Nguyen, K.N. Dinh, D. Simondson, S. Johnston, C. F. Garibello, D.A. Hoogeveen, B. Johannessen, D.R. MacFarlane, R.K. Hocking, M. Chatti, A.N. Simonov, Microwave-assisted synthesis of cobalt-based selenides as catalyst precursors for the alkaline water oxidation, *Adv. Energy Sustain. Res.* 4 (2023) 2300108, <https://doi.org/10.1002/aesr.202300108>.
- [40] Y. Wu, X. Tao, Y. Qing, H. Xu, F. Yang, S. Luo, C. Tian, M. Liu, X. Lu, Cr-Doped FeNi-P nanoparticles encapsulated into n-doped carbon nanotube as a robust bifunctional catalyst for efficient overall water splitting, *Adv. Mater.* 31 (2019) 1–9, <https://doi.org/10.1002/adma.201900178>.
- [41] J. Medina-Ramos, S.S. Lee, T.T. Fister, A.A. Hubaud, R.L. Sacci, D.R. Mullins, J. L. DiMeglio, R.C. Pupillo, S.M. Velardo, D.A. Lutterman, J. Rosenthal, P. Fenter, Structural dynamics and evolution of bismuth electrodes during electrochemical reduction of CO₂ in imidazolium-based ionic liquid solutions, *ACS Catal.* 7 (2017) 7285–7295, <https://doi.org/10.1021/acscatal.7b01370>.
- [42] L. Zhang, X. Wang, A. Li, X. Zheng, L. Peng, J. Huang, Z. Deng, H. Chen, Z. Wei, Rational construction of macroporous CoFeP triangular plate arrays from bimetal-organic frameworks as high-performance overall water-splitting catalysts, *J. Mater. Chem. A* 7 (2019) 17529–17535, <https://doi.org/10.1039/c9ta05282h>.
- [43] D. Song, H. Wang, X. Wang, B. Yu, Y. Chen, NiSe₂ nanoparticles embedded in carbon nanowires as highly efficient and stable electrocatalyst for hydrogen evolution reaction, *Electrochim. Acta* 254 (2017) 230–237, <https://doi.org/10.1016/j.electacta.2017.09.056>.
- [44] X. Xu, T. Liang, D. Kong, B. Wang, L. Zhi, Strain engineering of two-dimensional materials for advanced electrocatalysts, *Mater. Today Nano* 14 (2021) 100111, <https://doi.org/10.1016/j.mtnano.2021.100111>.
- [45] C. Di, D.T. Nguyen, T.L.L. Tran, N.H. Doan, J.H.L. Kim, Constructing MoP x @MnP y heteronanoparticle-supported mesoporous N, P-codoped graphene for boosting oxygen reduction and oxygen evolution reaction, *Chem. Mater.* 31 (2019) 2892–2904, <https://doi.org/10.1021/acs.chemmater.9b00071>.
- [46] B. Wang, Y. Hu, B. Yu, X. Zhang, D. Yang, Y. Chen, Heterogeneous CoFe–Co8Fe8S8 nanoparticles embedded in CNT networks as highly efficient and stable electrocatalysts for oxygen evolution reaction, *J. Power Sources* 433 (2019) 126688, <https://doi.org/10.1016/j.jpowsour.2019.05.094>.
- [47] G.A. Gebreslase, M.V. Martínez-Huerta, D. Sebastián, M.J. Lázaro, NiCoP/CoP sponge-like structure grown on stainless steel mesh as a high-performance electrocatalyst for hydrogen evolution reaction, *Electrochim. Acta* 438 (2023) 141538, <https://doi.org/10.1016/j.electacta.2022.141538>.
- [48] G.A. Gebreslase, D. Sebastián, M.V. Martínez-Huerta, T. Tsonecheva, B. Tsytarski, G. Georgiev, M.J. Lázaro, CoFe-loaded P, N co-doped carbon foam derived from petroleum pitch waste: an efficient electrocatalyst for oxygen evolution reaction, *Catal. Today* 423 (2023) 113991, <https://doi.org/10.1016/j.cattod.2022.12.022>.
- [49] Y. Wang, B. Kong, D. Zhao, H. Wang, C. Selomulya, Strategies for developing transition metal phosphides as heterogeneous electrocatalysts for water splitting, *Nano Today* 15 (2017) 26–55, <https://doi.org/10.1016/j.nantod.2017.06.006>.
- [50] Y. Wang, S. Zhao, Y. Zhu, R. Qiu, T. Gengenbach, Y. Liu, L. Zu, H. Mao, H. Wang, J. Tang, D. Zhao, C. Selomulya, Three-dimensional hierarchical porous nanotubes derived from metal-organic frameworks for highly efficient overall water splitting, *Sciencemag* 23 (2020) 100761, <https://doi.org/10.1016/j.isci.2019.100761>.
- [51] M. Zhang, J. Tu, M. Li, L. Zhi, 3D hierarchical porous N-doped carbon nanorarchitecture coated bimetallic phosphides as a highly efficient bifunctional electrocatalyst for overall water splitting, *J. Electroanal. Chem.* 961 (2024) 118224, <https://doi.org/10.1016/J.JELECHEM.2024.118224>.
- [52] Y. Dong, H. Wang, X. Wang, H. Wang, Q. Dong, W. Wang, X. Wei, J. Ren, J. Liu, R. Wang, Superhydrophilic/superaerophobic NiFe with internal bubble flow channels for electrocatalytic water splitting, *Chem. Eng. J.* 488 (2024) 150953, <https://doi.org/10.1016/j.cej.2024.150953>.
- [53] Y. Zhang, B. Chen, Y. Qiao, Y. Duan, X. Qi, S. He, H. Zhou, J. Chen, A. Yuan, S. Zheng, FeNi alloys incorporated N-doped carbon nanotubes as efficient bifunctional electrocatalyst with phase-dependent activity for oxygen and

- hydrogen evolution reactions, *J. Mater. Sci. Technol.* 201 (2024) 157–165, <https://doi.org/10.1016/j.jmst.2024.03.046>.
- [54] S. Chen, S.Z. Qiao, Hierarchically porous nitrogen-doped graphene-NiCo₂O₄ Hybrid Paper as an advanced electrocatalytic water-splitting material, *ACS Nano* 7 (2013) 10190–10196, <https://doi.org/10.1021/nn40444r>.
- [55] M. Gong, Y. Li, H. Wang, Y. Liang, J.Z. Wu, J. Zhou, J. Wang, T. Regier, F. Wei, H. Dai, An advanced Ni-Fe layered double hydroxide electrocatalyst for water oxidation, *J. Am. Chem. Soc.* 135 (2013) 8452–8455, <https://doi.org/10.1021/ja4027715>.
- [56] L. Trotochaud, S.L. Young, J.K. Ranney, S.W. Boettcher, Nickel-Iron oxyhydroxide oxygen-evolution electrocatalysts: the role of intentional and incidental iron incorporation, *J. Am. Chem. Soc.* 136 (2014) 6744–6753, <https://doi.org/10.1021/ja502379c>.
- [57] A. Mu, C. Scheu, A. Pokharel, S. Bo, T. Bein, D. Fattakhova-rohlfing, Iron-doped nickel oxide nanocrystals alkaline water splitting, *ACS Nano* 9 (2015) 5180–5188.
- [58] W. Ma, R. Ma, C. Wang, J. Liang, X. Liu, K. Zhou, T. Sasaki, A superlattice of alternately stacked Ni-Fe hydroxide nanosheets and graphene for efficient splitting of water, *ACS Nano* 9 (2015) 1977–1984, <https://doi.org/10.1021/nm5069836>.
- [59] Y. Zhao, X. Jia, G. Chen, L. Shang, G.J.N. Waterhouse, L.Z. Wu, C.H. Tung, D. Ohare, T. Zhang, Ultrafine NiO nanosheets stabilized by TiO₂ from monolayer NiTi-LDH precursors: an active water oxidation electrocatalyst, *J. Am. Chem. Soc.* 138 (2016) 6517–6524, <https://doi.org/10.1021/jacs.6b01606>.
- [60] X. He, F. Yin, Y. Li, H. Wang, J. Chen, Y. Wang, B. Chen, NiMnO₃/NiMn₂O₄ oxides synthesized via the aid of pollen: ilmenite/spinel hybrid nanoparticles for highly efficient bifunctional oxygen electrocatalysis, *ACS Appl. Mater. Interfaces* 8 (2016) 26740–26757, <https://doi.org/10.1021/acsmami.6b08101>.
- [61] H. Liang, A.N. Gardi, C. Xia, M.N. Hedhili, D.H. Anjum, U. Schwingenschlögl, H. N. Alshareef, Amorphous NiFe-OH/NiFeP electrocatalyst fabricated at low temperature for water oxidation applications, *ACS Energy Lett.* 2 (2017) 1035–1042, <https://doi.org/10.1021/acsenergylett.7b00206>.
- [62] X. Long, J. Li, S. Xiao, K. Yan, Z. Wang, H. Chen, S. Yang, A strongly coupled graphene and FeNi double hydroxide hybrid as an excellent electrocatalyst for the oxygen evolution reaction, *Angew. Chemie - Int. Ed.* 53 (2014) 7584–7588, <https://doi.org/10.1002/anie.201402822>.
- [63] C.Z. Yuan, Z.T. Sun, Y.F. Jiang, Z.K. Yang, N. Jiang, Z.W. Zhao, U.Y. Qazi, W. H. Zhang, A.W. Xu, One-step in situ growth of iron-nickel sulfide nanosheets on feni alloy foils: high-performance and self-supported electrodes for water oxidation, *Small* 13 (2017) 1–8, <https://doi.org/10.1002/smll.201604161>.
- [64] B.H.R. Suryanto, Y. Wang, R.K. Hocking, W. Adamson, C. Zhao, Overall electrochemical splitting of water at the heterogeneous interface of nickel and iron oxide, *Nat. Commun.* 10 (2019) 1–10, <https://doi.org/10.1038/s41467-019-13415-8>.
- [65] X. Li, H. Zhang, Q. Hu, W. Zhou, J. Shao, X. Jiang, C. Feng, H. Yang, C. He, Amorphous NiFe oxide-based nanoreactors for efficient electrocatalytic water oxidation, *Angew. Chemie - Int. Ed.* 62 (2023) e202300478.
- [66] Y.N. Wang, Z.J. Yang, D.H. Yang, L. Zhao, X.R. Shi, G. Yang, B.H. Han, FeCoP₂ nanoparticles embedded in N and P Co-doped hierarchically porous carbon for efficient electrocatalytic water splitting, *ACS Appl. Mater. Interfaces* 13 (2021) 8832–8843, <https://doi.org/10.1021/acsmami.0c22336>.
- [67] P. Geng, L. Wang, M. Du, Y. Bai, W. Li, Y. Liu, S. Chen, P. Braunstein, Q. Xu, H. Pang, MIL-96-Al for Li-S batteries: shape or size? *Adv. Mater.* 34 (2022) 1–10, <https://doi.org/10.1002/adma.202107836>.
- [68] W. Li, X. Guo, P. Geng, M. Du, Q. Jing, X. Chen, G. Zhang, H. Li, Q. Xu, P. Braunstein, H. Pang, Rational design and general synthesis of multimetallic metal-organic framework nano-octahedra for enhanced Li-S battery, *Adv. Mater.* 33 (2021) 1–9, <https://doi.org/10.1002/adma.202105163>.
- [69] O. Sato, T. Iyoda, A. Fujishima, K. Hashimoto, Photoinduced magnetization of a cobalt-iron cyanide, *Science* (80-.). 272 (1996) 704–705. doi: 10.1126/science.272.5262.704.
- [70] N. Ma, R. Ohtani, H.M. Le, S.S. Sørensen, R. Ishikawa, S. Kawata, S. Bureekaew, S. Kosasang, Y. Kawazoe, K. Ohara, M.M. Smedskjaer, S. Horike, Exploration of glassy state in Prussian blue analogues, *Nat. Commun.* 13 (2022) 1–11, <https://doi.org/10.1038/s41467-022-31658-w>.
- [71] J. Cattermull, S. Wheeler, K. Hurlbutt, M. Pasta, A.L. Goodwin, Filling vacancies in a Prussian blue analogue using mechanochemical post-synthetic modification, *Chem. Commun.* 56 (2020) 7873–7876, <https://doi.org/10.1039/d0cc02922j>.
- [72] A. Simonov, T. De Baerdemaeker, H.L.B. Boström, M.L. Ríos Gómez, H.J. Gray, D. Chernyshov, A. Bosak, H.B. Bürgi, A.L. Goodwin, Hidden diversity of vacancy networks in Prussian blue analogues, *Nature* 578 (2020) 256–260, <https://doi.org/10.1038/s41586-020-1980-y>.
- [73] Y. Xu, S. Zheng, H. Tang, X. Guo, H. Xue, H. Pang, Prussian blue and its derivatives as electrode materials for electrochemical energy storage, *Energy Storage Mater.* 9 (2017) 11–30, <https://doi.org/10.1016/j.ensm.2017.06.002>.
- [74] E.S. Goda, S. Lee, M. Sohail, K.R. Yoon, Prussian blue and its analogues as advanced supercapacitor electrodes, *J. Energy Chem.* 50 (2020) 206–229, <https://doi.org/10.1016/j.jechem.2020.03.031>.
- [75] P. Nie, J. Yuan, J. Wang, Z. Le, G. Xu, L. Hao, G. Pang, Y. Wu, H. Dou, X. Yan, X. Zhang, Prussian Blue analogue with fast kinetics through electronic coupling for sodium ion batteries, *ACS Appl. Mater. Interfaces* 9 (2017) 20306–20312, <https://doi.org/10.1021/acsmami.7b05178>.
- [76] M. Serhan, M. Sprawls, D. Jackemeyer, M. Long, I.D. Perez, W. Maret, N. Tao, E. Forzani, Total iron measurement in human serum with a smartphone, *J. Name* 00 (2013) 1–3, <https://doi.org/10.1039/x0xx00000x>.
- [77] Q. Wang, G. Xu, X. Liu, H. Ding, L. Zhang, Structure and surface optimization of NiFeP-based heterostructure immobilized on carbon nanotube for boosting electrocatalytic oxygen evolution, *J. Alloys Compd.* 997 (2024) 174957, <https://doi.org/10.1016/j.jallcom.2024.174957>.
- [78] Y. Shen, S.G. Guo, F. Du, X.B. Yuan, Y. Zhang, J. Hu, Q. Shen, W. Luo, A. Alsaedi, T. Hayat, G. Wen, G.L. Li, Y. Zhou, Z. Zou, Prussian blue analogue-derived Ni and Co bimetallic oxide nanoplate arrays block-built from porous and hollow nanocubes for the efficient oxygen evolution reaction, *Nanoscale* 11 (2019) 11765–11773, <https://doi.org/10.1039/c9nr01804b>.
- [79] L. Ji, Y. Wei, P. Wu, M. Xu, T. Wang, S. Wang, Q. Liang, T.J. Meyer, Z. Chen, Heterointerface engineering of Ni2P-Co2P nanoframes for efficient water splitting, *Chem. Mater.* 33 (2021) 9165–9173, <https://doi.org/10.1021/acscchemmater.1c02609>.
- [80] X. Wu, Y. Ru, Y. Bai, G. Zhang, Y. Shi, H. Pang, PBA composites and their derivatives in energy and environmental applications, *Coord. Chem. Rev.* 451 (2022) 214260, <https://doi.org/10.1016/j.ccr.2021.214260>.
- [81] G. Du, H. Pang, Recent advancements in Prussian blue analogues: preparation and application in batteries, *Energy Storage Mater.* 36 (2021) 387–408, <https://doi.org/10.1016/j.ensm.2021.01.006>.
- [82] L. Zhang, Z. Wan, J. Deng, F. Li, J. Dong, W. Yang, S. Xie, G. Li, F. Zhang, Catalytic membranes assembled by Co-Fe Prussian blue analogues functionalized graphene oxide nanosheets for rapid removal of contaminants, *J. Membr. Sci.* 705 (2024) 122886, <https://doi.org/10.1016/j.jmemsci.2024.122886>.
- [83] W.T. Chen, C.F. Yan, C.J. Yu, Y.C. Liao, C.F. Chen, Highly catalytic Prussian blue analogues and their application on the three-dimensional origami paper-based sweat sensors, *Biosens. Bioelectron.* 254 (2024) 116188, <https://doi.org/10.1016/j.bios.2024.116188>.
- [84] K. Lin, Z. He, L. Shen, J. Su, Z. Huang, Y. Xia, Y. Wang, Zinc-substituted Fe-based Prussian blue analogues induce a weak Jahn-Teller effect to enhance stability of sodium ion batteries, *J. Energy Storage* 90 (2024) 111924, <https://doi.org/10.1016/j.est.2024.111924>.
- [85] H.S. Han, S.J. Kim, S.Y. Jung, D. Oh, A.K. Nayak, J.U. Jang, J. Bang, S. Yeo, T. H. Shin, Amorphous-crystalline interfaces on hollow nanocubes derived from Ir-doped Ni-Fe-Zn Prussian Blue analog enables high capability of alkaline/acidic/saline water oxidations, *Small* 19 (2023) 1–11, <https://doi.org/10.1002/smll.202303912>.
- [86] S. Park, J.H. Jun, M. Park, J. Jeong, J.H. Jo, S. Jeon, J. Yang, S.M. Choi, W. Jo, J. H. Lee, Hierarchically designed Co₄Fe₃@N-doped graphitic carbon as an electrocatalyst for oxygen evolution in anion-exchange-membrane water electrolysis, *Energy and Fuels* 38 (2024) 4451–4463, <https://doi.org/10.1021/acs.energyfuels.3c04077>.
- [87] S. Ibraheem, S. Chen, J. Li, W. Li, X. Gao, Q. Wang, Z. Wei, Three-dimensional Fe, N-decorated carbon-supported NiFeP nanoparticles as an efficient bifunctional catalyst for rechargeable Zinc-O₂ batteries, *ACS Appl. Mater. Interfaces* 11 (2019) 699–705, <https://doi.org/10.1021/acsmami.8b16126>.
- [88] Z. Wu, L. Li, J.M. Yan, X.B. Zhang, Materials design and system construction for conventional and new-concept supercapacitors, *Adv. Sci.* 4 (2017) 1600382, <https://doi.org/10.1002/advs.201600382>.
- [89] C.C.L. McCrory, S. Jung, J.C. Peters, T.F. Jaramillo, Benchmarking heterogeneous electrocatalysts for the oxygen evolution reaction, *J. Am. Chem. Soc.* 135 (2013) 16977–16987, <https://doi.org/10.1021/ja407115p>.
- [90] I.S. Filimonenkov, C. Bouillet, G. Kéranguéven, P.A. Simonov, G.A. Tsirlina, E. R. Savinova, Carbon materials as additives to the OER catalysts: RRDE study of carbon corrosion at high anodic potentials, *Electrochim. Acta* 321 (2019) 134657, <https://doi.org/10.1016/j.electacta.2019.134657>.
- [91] I. Gatto, A. Capri, C. Lo Vecchio, S. Zignani, A. Patti, V. Baglio, Optimal operating conditions evaluation of an anion-exchange-membrane electrolyzer based on FUMASEP® FAAs-50 membrane, *Int. J. Hydrogen Energy* 48 (2022) 11914–11921, <https://doi.org/10.1016/j.ijhydene.2022.04.176>.
- [92] M. Chen, M. Mandal, K. Groenhout, G. McCool, H.M. Tee, B. Zulevi, P.A. Kohl, Self-adhesive ionomers for durable low-temperature anion exchange membrane electrolysis, *J. Power Sources* 536 (2022) 231495, <https://doi.org/10.1016/j.jpowsour.2022.231495>.
- [93] Y. Zeng, G.F. Chen, Z. Jiang, L.X. Ding, S. Wang, H. Wang, Confined heat treatment of a Prussian blue analogue for enhanced electrocatalytic oxygen evolution, *J. Mater. Chem. A* 6 (2018) 15942–15946, <https://doi.org/10.1039/c8ta05677c>.
- [94] E. Vijayakumar, S. Ramakrishnan, C. Sathiskumar, D. Jin, J. Balamurugan, H. Sung, D. Kwon, Y. Hoon, H. Lee, MOF-derived CoP-nitrogen-doped carbon @ NiFeP nanoflakes as an efficient and durable electrocatalyst with multiple catalytically active sites for OER , HER , ORR and rechargeable zinc-air batteries, *428* (2022) 131115.
- [95] C. Lai, H. Li, Y. Sheng, M. Zhou, W. Wang, M. Gong, K. Wang, K. Jiang, 3D Spatial combination of CN vacancy-mediated nife-PBA with N-doped carbon nanofibers network toward free-standing bifunctional electrode for Zn-Air batteries, *Adv. Sci.* 9 (2022) 1–10, <https://doi.org/10.1002/advs.202105925>.
- [96] T. Zhang, J. Du, P. Xi, C. Xu, Hybrids of Cobalt/iron phosphides derived from bimetal-organic frameworks as highly efficient electrocatalysts for oxygen evolution reaction, *ACS Appl. Mater. Interfaces* 9 (2017) 362–370, <https://doi.org/10.1021/acsami.6b12189>.
- [97] S. García-Dalf, J. Quílez-Bermejo, J. Castro-Gutiérrez, N. Baccile, M.T. Izquierdo, A. Celzard, V. Fierro, Green and easy synthesis of P-doped carbon-based hydrogen evolution reaction electrocatalysts, *Carbon* n. y. 212 (2023) 118154, <https://doi.org/10.1016/j.carbon.2023.118154>.

- [98] M. Gao, W. Sheng, Z. Zhuang, Q. Fang, S. Gu, J. Jiang, Y. Yan, Efficient water oxidation using nanostructured α -nickel-hydroxide as an electrocatalyst, *J. Am. Chem. Soc.* 136 (2014) 7077–7084, <https://doi.org/10.1021/ja502128j>.
- [99] T.D. Nguyen, G.G. Scherer, Z.J. Xu, A facile synthesis of size-controllable IrO_2 and RuO_2 nanoparticles for the oxygen evolution reaction, *Electrocatalysis* 7 (2016) 420–427, <https://doi.org/10.1007/s12678-016-0321-2>.
- [100] C. Yang, C. Laberty-Robert, D. Batuk, G. Cibin, A.V. Chadwick, V. Pimenta, W. Yin, L. Zhang, J.M. Tarascon, A. Grimaud, Phosphate ion functionalization of perovskite surfaces for enhanced oxygen evolution reaction, *J. Phys. Chem. Lett.* 8 (2017) 3466–3472, <https://doi.org/10.1021/acs.jpclett.7b01504>.
- [101] J.T. Mefford, X. Rong, A.M. Abakumov, W.G. Hardin, S. Dai, A.M. Kolpak, K. P. Johnston, K.J. Stevenson, Water electrolysis on $\text{La}_{1-x}\text{Sr}_x\text{CoO}_3\delta$ perovskite electrocatalysts, *Nat. Commun.* 7 (2016) 11053, <https://doi.org/10.1038/ncomms11053>.
- [102] D. Antipin, M. Risch, Calculation of the Tafel slope and reaction order of the oxygen evolution reaction between pH 12 and pH 14 for the adsorbate mechanism, *Electrochim. Sci. Adv.* (2022) 1–13, <https://doi.org/10.1002/elsa.202100213>.
- [103] I.C. Man, H.Y. Su, F. Calle-Vallejo, H.A. Hansen, J.I. Martínez, N.G. Inoglu, J. Kitchin, T.F. Jaramillo, J.K. Nørskov, J. Rossmeisl, Universality in oxygen evolution electrocatalysis on oxide surfaces, *ChemCatChem* 3 (2011) 1159–1165, <https://doi.org/10.1002/cctc.201000397>.
- [104] F. Zhao, X. Mao, X. Zheng, H. Liu, L. Zhu, W. Li, Z. Wang, H. Chen, Roles of the self-reconstruction layer in the catalytic stability of a NiFeP catalyst during the oxygen evolution reaction, *J. Mater. Chem. A* 11 (2023) 276–286, <https://doi.org/10.1039/d2ta06514b>.
- [105] S. Liang, B. Wei, M. Yuan, Y. Li, X. Ma, Y. Wu, L. Xu, Self-supported reevesite Ni-Fe layered double hydroxide nanosheets arrays for efficient water oxidation, *ChemistrySelect* 5 (2020) 3062–3068, <https://doi.org/10.1002/slct.202000151>.
- [106] W. Zou, C. Sun, K. Zhao, J. Li, X. Pan, D. Ye, Y. Xie, W. Xu, H. Zhao, L. Zhang, J. Zhang, Surface reconstruction of NiCoP pre-catalysts for bifunctional water splitting in alkaline electrolyte, *Electrochim. Acta* 345 (2020) 136114, <https://doi.org/10.1016/j.electacta.2020.136114>.
- [107] S. Nagappan, A. Karmakar, R. Madhu, S.S. Selvasundarasekar, S. Kumaravel, K. Bera, H.N. Dhandapani, D. Sarkar, S.M. Yusuf, S. Kundu, 2D CoFe-LDH nanosheet-incorporated 1D microfibers as a high-performance OER electrocatalyst in neutral and alkaline media, *ACS Appl. Energy Mater.* 5 (2022) 11483–11497, <https://doi.org/10.1021/acsaeam.2c01964>.
- [108] L. Yaqoob, T. Noor, N. Iqbal, H. Nasir, N. Zaman, K. Talha, Electrochemical synergies of Fe-Ni bimetallic MOF CNTs catalyst for OER in water splitting, *J. Alloys Compd.* 850 (2021) 156583, <https://doi.org/10.1016/j.jallcom.2020.156583>.
- [109] L. Shen, Q. Zhang, J. Luo, H.C. Fu, X.H. Chen, L.L. Wu, H.Q. Luo, N.B. Li, Fabrication of 2D/3D hierarchical PBA and derivative electrocatalysts for overall water splitting, *Appl. Surf. Sci.* 551 (2021) 149360, <https://doi.org/10.1016/j.apusc.2021.149360>.
- [110] X. Lin, S. Cao, H. Chen, X. Chen, Z. Wang, S. Zhou, H. Xu, S. Liu, S. Wei, X. Lu, Boosting oxygen evolution reaction of hierarchical spongy NiFe-PBA/Ni₃C(B) electrocatalyst: interfacial engineering with matchable structure, *Chem. Eng. J.* 433 (2022) 133524, <https://doi.org/10.1016/j.cej.2021.133524>.
- [111] O. Ambriz-Peláez, J. Béjar, C.M. Ramos-Castillo, M. Guerra-Balcázar, L. Álvarez-Contreras, N. Arjona, Defected NiFe layered double hydroxides on N-doped carbon nanotubes as efficient bifunctional electrocatalyst for rechargeable zinc-air batteries, *Appl. Surf. Sci.* 601 (2022) 154253, <https://doi.org/10.1016/j.apusc.2022.154253>.
- [112] D. Lin, A. Lasia, Electrochemical impedance study of the kinetics of hydrogen evolution at a rough palladium electrode in acidic solution, *J. Electroanal. Chem.* 785 (2017) 190–195, <https://doi.org/10.1016/j.jelechem.2016.12.037>.
- [113] F.R. Costa, D.V. Franco, L.M. Da Silva, Electrochemical impedance spectroscopy study of the oxygen evolution reaction on a gas-evolving anode composed of lead dioxide microfibers, *Electrochim. Acta* 90 (2013) 332–343, <https://doi.org/10.1016/j.electacta.2012.12.043>.
- [114] Z. Liang, W. Zhou, S. Gao, R. Zhao, H. Zhang, Y. Tang, J. Cheng, T. Qiu, B. Zhu, C. Qu, W. Guo, Q. Wang, R. Zou, Fabrication of hollow CoP/TiO_x heterostructures for enhanced oxygen evolution reaction, *Small* 16 (2020) 1–10, <https://doi.org/10.1002/smll.201905075>.
- [115] L.M. Behrooz Motealleh, Z. Liu, R.J. Masel, J.P. Sculley, Zheng Richard Ni, Next-generation anion exchange membrane water electrolyzers operating for commercially relevant lifetimes, *Int. J. Hydrogen Energy* 49 (2020) 3379–3386.
- [116] J.E. Park, S. Bin Park, M.J. Kim, H. Shin, S.Y. Kang, Y.H. Cho, Y.E. Sung, Three-dimensional unified electrode design using a NiFeOOH catalyst for superior performance and durable anion-exchange membrane water electrolyzers, *ACS Catal.* 12 (2022) 135–145, <https://doi.org/10.1021/acscatal.1c04117>.
- [117] A. Capri, I. Gatto, C. Lo Vecchio, V. Baglio, Effect of the calcination temperature on the characteristics of Ni/Fe-oxide electrocatalysts for application in anion exchange membrane electrolyzers, *Ind. Chem. Mater.* 1 (2023) 553–562, <https://doi.org/10.1039/d3im00065f>.
- [118] Z. Liu, S.D. Sajjad, Y. Gao, H. Yang, J.J. Kaczur, R.I. Masel, The effect of membrane on an alkaline water electrolyzer, *Int. J. Hydrogen Energy* 42 (2017) 29661–29665, <https://doi.org/10.1016/j.ijhydene.2017.10.050>.
- [119] J.E. Park, M.J. Kim, M.S. Lim, S.Y. Kang, J.K. Kim, S.H. Oh, M. Her, Y.H. Cho, Y. E. Sung, Graphitic carbon nitride-carbon nanofiber as oxygen catalyst in anion-exchange membrane water electrolyzer and rechargeable metal-air cells, *Appl. Catal. B Environ.* 237 (2018) 140–148, <https://doi.org/10.1016/j.apcatb.2018.05.073>.
- [120] A. Carbone, S.C. Zignani, I. Gatto, S. Trocino, A.S. Aricò, Assessment of the FAA3-50 polymer electrolyte in combination with a NiMn₂O₄ anode catalyst for anion exchange membrane water electrolysis, *Int. J. Hydrogen Energy* 45 (2020) 9285–9292, <https://doi.org/10.1016/j.ijhydene.2020.01.150>.
- [121] C. Busacca, S.C. Zignani, A. Di Blasi, O. Di Blasi, M. La Faro, V. Antonucci, A. S. Aricò, Electrospun NiMn₂O₄ and NiCo₂O₄ spinel oxides supported on carbon nanofibers as electrocatalysts for the oxygen evolution reaction in an anion exchange membrane-based electrolysis cell, *Int. J. Hydrogen Energy* 44 (2019) 20987–20996, <https://doi.org/10.1016/j.ijhydene.2019.02.214>.
- [122] I.V. Pushkareva, A.S. Pushkarev, S.A. Grigoriev, P. Modisha, D.G. Bessarabov, Comparative study of anion exchange membranes for low-cost water electrolysis, *Int. J. Hydrogen Energy* 45 (2020) 26070–26079, <https://doi.org/10.1016/j.ijhydene.2019.11.011>.
- [123] B. Motealleh, Z. Liu, R.I. Masel, J.P. Sculley, Z. Richard Ni, L. Meroueh, Next-generation anion exchange membrane water electrolyzers operating for commercially relevant lifetimes, *Int. J. Hydrogen Energy* 46 (2021) 3379–3386, <https://doi.org/10.1016/j.ijhydene.2020.10.244>.
- [124] C. Li, J.B. Baek, The promise of hydrogen production from alkaline anion exchange membrane electrolyzers, *Nano Energy* 87 (2021) 106162, <https://doi.org/10.1016/j.nanoen.2021.106162>.
- [125] D. Li, A.R. Motz, C. Bae, C. Fujimoto, G. Yang, F.Y. Zhang, K.E. Ayers, Y.S. Kim, Durability of anion exchange membrane water electrolyzers, *Energy Environ. Sci.* 14 (2021) 3393–3419, <https://doi.org/10.1039/d0ee04086j>.
- [126] J.A. Macía-Agulló, D. Cazorla-Amorós, A. Linares-Solano, U. Wild, D.S. Su, R. Schlögl, Oxygen functional groups involved in the styrene production reaction detected by quasi *in situ* XPS, *Catal. Today* 102–103 (2005) 248–253, <https://doi.org/10.1016/j.cattod.2005.02.023>.
- [127] S. Campagna Zignani, M. Lo Faro, A. Carbone, C. Italiano, S. Trocino, G. Monforte, A.S. Aricò, Performance and stability of a critical raw materials-free anion exchange membrane electrolysis cell, *Electrochim. Acta* 413 (2022) 140078, <https://doi.org/10.1016/j.electacta.2022.140078>.
- [128] X. Luo, D.I. Kushner, J. Li, E.J. Park, Y.S. Kim, A. Kusoglu, Anion exchange ionomers: impact of chemistry on thin-film properties, *Adv. Funct. Mater.* 31 (2021) 1–12, <https://doi.org/10.1002/adfm.202000878>.
- [129] Y.S. Kim, Polymer electrolytes with high ionic concentration for fuel cells and electrolyzers, *ACS Appl. Polym. Mater.* 3 (2021) 1250–1270, <https://doi.org/10.1021/acsapm.0c01405>.
- [130] A.N. Colli, H.H. Girault, A. Battistel, Non-precious electrodes for practical alkaline water electrolysis, *Materials (Basel)* 12 (2019) 1–17, <https://doi.org/10.3390/ma12081336>.
- [131] D. Aili, M.R. Kraglund, J. Tavacoli, C. Chatzichristodoulou, J.O. Jensen, Polysulfone-polyvinylpyrrolidone blend membranes as electrolytes in alkaline water electrolysis, *J. Membr. Sci.* 598 (2020) 117674, <https://doi.org/10.1016/j.memsci.2019.117674>.
- [132] A.K. Niaz, A. Akhtar, J.Y. Park, H.T. Lim, Effects of the operation mode on the degradation behavior of anion exchange membrane water electrolyzers, *J. Power Sources* 481 (2021) 229093, <https://doi.org/10.1016/j.jpowsour.2020.229093>.
- [133] F. Razmjooei, T. Morawietz, E. Taghizadeh, E. Hadjixenophontos, L. Mues, M. Gerle, B.D. Wood, C. Harms, A.S. Gago, S.A. Ansar, K.A. Friedrich, Increasing the performance of an anion-exchange membrane electrolyzer operating in pure water with a nickel-based microporous layer, *Joule* 5 (2021) 1776–1799, <https://doi.org/10.1016/j.joule.2021.05.006>.
- [134] X. Hu, R. Wang, W. Feng, C. Xu, Z. Wei, Electrocatalytic oxygen evolution activities of metal chalcogenides and phosphides: Fundamentals, origins, and future strategies, *J. Energy Chem.* 81 (2023) 167–191, <https://doi.org/10.1016/j.jecchem.2023.01.062>.
- [135] J. Yang, M.J. Jang, X. Zeng, Y.S. Park, J. Lee, S.M. Choi, Y. Yin, Non-precious electrocatalysts for oxygen evolution reaction in anion exchange membrane water electrolysis: a mini review, *Electrochim. Commun.* 131 (2021) 107118, <https://doi.org/10.1016/j.elecom.2021.107118>.